



Long-term X-ray observations of seyfert 1 galaxy ark 120: on the origin of soft-excess

Prantik Nandi¹,¹★ Arka Chatterjee^{1,2,3}★ Sandip K. Chakrabarti⁴ and Broja G. Dutta^{4,5}

¹Department of Astrophysics & Cosmology, S. N. Bose National Centre for Basic Science, Salt lake, Sector III, Kolkata 700091, India

²Department of Physics, School of Natural Sciences, UNIST, Ulsan 44919, Republic of Korea

³Department of Astronomy and Space Science, Chungbuk National University, Cheongju 361-763, Republic of Korea

⁴Indian Centre for Space Science, Garia Station Road, Kolkata 700084, India

⁵Department of Physics, Rishi Bankim Chandra College, Naihati 743165, India

Accepted 2021 June 10. Received 2021 June 8; in original form 2020 December 9

ABSTRACT

We present the long-term X-ray spectral and temporal analysis of a ‘bare-type AGN’ Ark 120. We consider the observations from *XMM–Newton*, *Suzaku*, *Swift*, and *NuSTAR* from 2003 to 2018. The spectral properties of this source are studied using various phenomenological and physical models present in the literature. We report (a) the variations of several physical parameters, such as the temperature and the optical depth of the electron cloud, the size of the Compton cloud, and the accretion properties for the last 15 yr. The spectral variations are explained from the changes in the accretion dynamics; (b) the X-ray time delay between 0.2–2 and 3–10 keV light-curves exhibited *zero-delay* in 2003, *positive delay* of 4.71 ± 2.1 ks in 2013, and *negative delay* of 2.90 ± 1.26 ks in 2014. The delays are explained considering Comptonization, reflection, and light-crossing time; (c) the long-term intrinsic luminosities, obtained using *nthcomp*, of the soft-excess and the primary continuum show a correlation with a Pearson correlation coefficient of 0.90. This indicates that the soft-excess and the primary continuum originate from the same physical process. From a physical model fitting, we infer that the soft excess for Ark 120 could be due to a small number of scatterings in the Compton cloud. Using Monte Carlo simulations, we show that indeed the spectra corresponding to fewer scatterings could provide a steeper soft-excess power law in the 0.2–3 keV range. Simulated luminosities are found to be in agreement with the observed values.

Key words: galaxies: active – galaxies: Seyfert – X-rays: galaxies – X-rays: individual: Ark 120.

1 INTRODUCTION

Active galactic nuclei (AGNs) are the most energetic phenomena in the universe. The emitted radiation is observed over the entire range of the electromagnetic spectrum. The high energy X-rays are believed to be emitted from the innermost region of an accretion disc, which surrounds the central black hole (Pringle, Rees & Pacholczyk 1973; Shakura & Sunyaev 1973). The X-ray spectra of Seyfert 1 galaxies, a subclass of AGNs, is mostly fitted by a power-law component with photon index in the range $\Gamma = 1.6$ – 2.2 (Bianchi et al. 2009; Sobolewska & Papadakis 2009; Laha, Dewangan & Kembhavi 2011) and a high energy cut-off. The spectral contribution which deviates from the power-law at lower energy (below ~ 2 keV) is known as ‘soft excess’ (Halpern 1984; Arnaud et al. 1985; Singh, Garmire & Nousek 1985). The X-ray spectra are often associated with a Fe $K\alpha$ line, which is observed near 6.4 keV, and a Compton hump in the energy range of 20.0 to 40.0 keV. It has been observed that the primary power-law emission is produced by the Comptonization of low-energy seed photons (Sunyaev & Titarchuk 1980; Titarchuk 1994) emitted from the standard Keplerian disc. The seed photons are processed from the accretion mechanism, and the peak emission arises at optical/ultraviolet (UV) wavelengths (Pringle et al. 1973) for

a supermassive black hole (SMBH). However, the location, as well as the geometry of the Compton reprocessing region, are still a matter of debate. This Compton cloud can be situated above the accretion disc (Haardt & Maraschi 1991, 1993; Poutanen & Svensson 1996) or at the base of the relativistic jet (Chakrabarti & Titarchuk 1995; Fender et al. 1999; Fender, Belloni & Gallo 2004; Markoff, Nowak & Wilms 2005). The region could be a hot, radiatively inefficient and behave like a quasi-Bondi flow as discussed initially by Ichimaru (1977). This region could originate the thermal Comptonization of soft photons produced in the optical/UV range from an optically thick Keplerian disc (Magdziarz et al. 1998; Dewangan et al. 2007; Done et al. 2012; Lohfink et al. 2012) or a blurred reflection from ionized disc (Fabian et al. 2002; Ross & Fabian 2005; Crummy et al. 2006; García et al. 2014). The iron line is thought to be originated by the photoelectric absorption followed by the fluorescence line emission from a dense and relatively cold accretion disc. Moreover, it is believed that the Compton hump could be due to the Compton scattering dominated above 10 keV in a relatively cold dense medium. Nevertheless, the complex broad-band spectrum of AGNs requires a proper physical explanation of the flow dynamics and radiative properties around the central engine across the soft and hard energy regime of the X-ray.

In this scenario, the two-component advective flow (TCAF) (Chakrabarti & Titarchuk 1995) model, which combines the essence of all the salient features of a viscous transonic flow (Chakrabarti

* E-mail: prantiknandi007@gmail.com (PN); arka019icsp@gmail.com (AC)

1989, 1990, 1995) around black holes is worth exploring. It is a physical solution encompassing hydrodynamics and radiative processes. The transonic flow solution allows two types of accretion flows depending on how efficiently angular momentum is being transported: a viscous, geometrically thin, optically thick standard Keplerian component (Shakura & Sunyaev 1973) and a weakly viscous, geometrically thick, optically thin sub-Keplerian halo component (Chakrabarti & Titarchuk 1995). The latter is basically an inefficiently radiating generalized Bondi flow with high radial velocity until it forms the centrifugal barrier after which it becomes efficient in radiating at higher energies due to inverse Comptonization. The Keplerian disc is formally truncated at the centrifugal barrier, the outer boundary of which is the shock location (Chakrabarti 1989). The post-shock region (i.e. the region between the shock and the innermost sonic point) is known as the CENTrifugal barrier supported BOUNDary Layer or CENBOL and it acts as the Compton cloud. The soft photons from the Keplerian disc are upscattered by Comptonization process in the post-shock region and produce the high energy X-ray photons. TCAF, a self-consistent model, is quantified by four flow parameters: two types of accretion rates, namely, the disc rate (\dot{m}_d) and halo rate (\dot{m}_h), size and density of the Compton cloud, through the shock location (X_s) and the compression ratio (R), ratio of the post-shock and the pre-shock flow densities ($\frac{\rho_+}{\rho_-}$). It also requires an intrinsic parameter, namely, the mass of the central black hole (in the units of M_\odot), and an extrinsic parameter, namely, the normalization which is required to place the observed spectrum over the theoretical spectrum of TCAF. The broad-band spectra of M87 were explained with this model by fitting the data from multiwavelength observations (Mandal & Chakrabarti 2008). Later, TCAF has been implemented in *xspec* (Arnaud 1996) as a local table model and has been successful to fit the data of the Galactic black holes (Debnath, Chakrabarti & Mondal 2014) and has also been able to estimate the mass of nearby Seyfert 1 galaxy NGC 4151 using *NuSTAR* data (Nandi, Chakrabarti & Mondal 2019).

Arakelian 120 (Ark 120) is a nearby ($z = 0.03271^1$) radio-quiet Seyfert 1 AGN with radio-loudness $R \approx 0.1$ (Condon et al. 1998; Ho 2002). This source was intensely monitored nearly in all wavelengths: optical/UV (Kollatschny et al. 1981; Kollatschny et al. 1981; Schulz & Rafanelli 1981; Alloin, Boisson & Pelat 1988; Marziani, Calvani & Sulentic 1992; Peterson et al. 1998; Stanic et al. 2000; Popović et al. 2001; Doroshenko, Sergeev & Pronik 2008; Kuehn et al. 2008) and X-ray (Vaughan et al. 2004; Nardini et al. 2016; Reeves et al. 2016; Gliozzi et al. 2017; Lobban et al. 2018) and was found to be consistently bright in optical, UV, and X-rays displaying substantial wavelength-dependent variability (Gliozzi et al. 2017; Lobban et al. 2018). From the simultaneous UV/X-ray measurements, it was reported that the observations are neither ‘contaminated’ by absorption signatures along the line of sight (Crenshaw et al. 1999; Vaughan et al. 2004; Reeves et al. 2016) nor by neutral intrinsic absorbers (Reeves et al. 2016) around the central engine. Furthermore, Ark 120 is nearly free from intrinsic reddening in the IR–optical–UV continuum (Ward et al. 1987; Vasudevan et al. 2009). The X-ray spectra of Ark 120 does not exhibit any ionized absorption (Laha et al. 2014, 2016) and see for a review on ionized outflows Laha et al. (2021).

Therefore, these provide one of the cleanest views ($N_H \sim 3 \times 10^{19} \text{ cm}^{-2}$; (Vaughan et al. 2004)) of the central region. These types of

AGNs are called ‘bare nucleus’ Seyferts or bare AGNs. It should be noted that, using *XMM–Newton*/RGS data, Reeves et al. (2016) found ionized medium surrounding at least 10 per cent of the nuclear region of Ark 120. However, the intervening medium is most likely to be out of our line of sight. The estimated mass of the central black hole of Ark 120 is $M_{\text{BH}} = 1.50 \pm 0.19 \times 10^8 M_\odot$ (Peterson et al. 2004), which was measured using the reverberation-mapping technique. From the spectroscopic monitoring data of Ark 120 during 1976 to 2013 using a 70-cm telescope, Denissyuk, Valiullin & Gaisina (2015) estimated the mass of the central SMBH to be $M_{\text{BH}} = 1.675 \pm 0.028 \times 10^8 M_\odot$. This source has a low Eddington ratio of $L_{\text{bol}}/L_E \sim 0.05$ (Vasudevan & Fabian 2007) with a strong soft-excess (Matt et al. 2014; Porquet et al. 2004, 2019) and a significant broad Fe K_α line (Vaughan et al. 2004; Nardini et al. 2011, 2016). Nardini et al. (2011) analyzed Ark 120 spectra, where, in the absence of an absorber of complex morphology, soft-excess was explained by reflection from the centrally located hot and cold medium located at a distance. Marinucci et al. (2019) used the Monte Carlo technique to investigate the favourable shape of the Compton cloud considering the future polarimetric missions such as *IXPE* (Weisskopf et al. 2016).

Although Ark 120 is a widely studied source, the evolution of the X-ray spectra over the last two decades is yet to be understood. A steepening of the X-ray spectrum was observed during six-month monitoring in 2014 with *Swift*. The observed spectral variability was attributed to the possible existence of a large disc reprocessing region (Gliozzi et al. 2017). Again during 2017–2018, a longer time delay was observed (Lobban et al. 2018) between long-wavelength difference (i.e. optical and X-ray). They predicted that the accretion disc could exist in a longer scale as predicted by standard accretion disc theory. The soft-excess part of Ark 120 could be originated due to the Comptonization within the hot electron cloud of various shape (Marinucci et al. 2019), reflection from a cold medium (Nardini et al. 2011) or the shock heating near the inner edge of the disc (Fukumura et al. 2016). We analyzed the long-term X-ray archival data of Ark 120 which provides an ideal testbed to understand the soft-excess as well as its interaction with the harder ($> 2 \text{ keV}$) photons. Along with the observations, we perform Monte Carlo simulations to find the effect of Comptonization within the energy range of soft-excess. We also study the X-ray variability of the source over a longer period and to calculate the approximate time-delays in X-ray bands. For the first time, we also find the flow and system parameters by fitting of the X-ray data. The paper is structured in the following way: In Section 2, we provide the details of the observational data and their reduction procedure. The results of the spectral and temporal analysis are presented in Section 3 and 4. We discuss our findings in Section 5 and finally, draw our conclusions in Section 6.

2 OBSERVATION AND DATA REDUCTION

We use the publicly available archival data of *XMM–Newton*, *NuSTAR*, *Swift*, and *Suzaku* using HEASARC.² We reprocessed all data using HEASOFT v6.26.1 (Arnaud 1996), which includes XSPEC v12.10.1f.

2.1 XMM–Newton

Ark 120 has been observed by *XMM–Newton* (Jansen et al. 2001) during three epochs from 2003 to 2014. In 2003 and 2013, it has made

¹The redshift is taken from the NASA/Infrared Process and Analysis center (IPAC) Extragalactic Database. <https://ned.ipac.caltech.edu>

²<http://heasarc.gsfc.nasa.gov/>

Table 1. Observation log: We used the cross-normalization factor, $N_{\text{FPMA}} = 1.0$, $N_{\text{FPMB}} = 0.98 \pm 0.05$, $N_{\text{EPIC/pn}} = 0.93 \pm 0.01$, $N_{\text{XIS03}} = 1.005 \pm 0.01$, $N_{\text{HDX}} = 1.12 \pm 0.03$, and $N_{\text{XRT}} = 1.04 \pm 0.03$ (Madsen et al. 2015) for average count rate corrections. The count rates and fluxes are calculated for the energy range of 0.5–10.0 keV.

ID	Date	Observation ID	Instrument	Exposures	Mean count	Flux
	(yyyy-mm-dd)			(ks)	(count s ⁻¹)	(10 ⁻¹¹ erg cm ⁻² s ⁻¹)
XMM1	2003-08-24	0147190101	<i>XMM-Newton</i> /EPIC-pn	112.15	16.75 ± 0.02	6.86
S1	2007-04-01	702014010	<i>Suzaku</i> /XIS-HXD	100.86	7.62 ± 0.003	58.2
XRT1	2008-07-24 –2008-08-03	00037593001 –00037593003	<i>Swift</i> /XRT	10.86	1.74 ± 0.79	4.33
XMM2	2013-02-18	0693781501	<i>XMM-Newton</i> /EPIC-pn	130.46	7.97 ± 0.02	3.80
N1	2013-02-18	60001044002	<i>NuSTAR</i> /FPMA	55.33	0.97 ± 0.09	1.91 ^a
N1	2013-02-18	60001044002	<i>NuSTAR</i> /FPMB	55.33	0.94 ± 0.09	1.90 ^a
XMM3/a	2014-03-18	0721600201	<i>XMM-Newton</i> /EPIC-pn	132.7	23.14 ± 0.02	6.13
XMM3/b	2014-03-20	0721600301	<i>XMM-Newton</i> /EPIC-pn	131.8	19.49 ± 0.02	6.81
XMM3/c	2014-03-22	0721600401	<i>XMM-Newton</i> /EPIC-pn	133.3	16.11 ± 0.02	6.24
N2	2014-03-22	60001044004	<i>NuSTAR</i> /FPMA	65.45	1.48 ± 0.07	3.07 ^a
N2	2014-03-22	60001044004	<i>NuSTAR</i> /FPMB	65.45	1.53 ± 0.07	3.07 ^a
XMM3/d	2014-03-24	0721600501	<i>XMM-Newton</i> /EPIC-pn	133.3	19.66 ± 0.02	6.33
XRT2	2014-09-04 –2014-10-19	00091909002 –00091909022	<i>Swift</i> /XRT	22.81	1.34 ± 0.08	4.27
XRT3	2014-10-22 –2014-12-05	00091909023 –00091909044	<i>Swift</i> /XRT	20.18	1.59 ± 0.11	4.66
XRT4	2014-12-09 –2015-01-26	00091909045 –00091909068	<i>Swift</i> /XRT	23.48	1.43 ± 0.09	4.29
XRT5	2015-01-26 –2015-03-15	00091909069 –00091909090	<i>Swift</i> /XRT	21.66	1.44 ± 0.08	4.16
XRT6	2017-12-07 –2018-01-24	00010379001 –00010379048	<i>Swift</i> /XRT	44.14	1.13 ± 0.08	3.08

^aFlux is calculated for the energy range 3.0 to 10.0 keV.

~112 (XMM1) and ~130 ks (XMM2) observations, respectively. The XMM1 data is used by (Vaughan et al. 2004) and reported that the source Ark 120 is one of the cleanest Sy1 type AGNs. In 2014, *XMM-Newton* observed Ark 120 four times between March 18 and March 24. Out of these, one (XMM3) was simultaneous with *NuSTAR* observation. The details of the observation log are presented in Table 1. It was observed that the X-ray flux of this source was about a factor of two higher in 2014 than the XMM2 observation (Matt et al. 2014; Marinucci et al. 2019) made in 2013. A similar trend of flux variation was also reported in optical/UV (Lobban et al. 2018) band.

Due to the high brightness of the source, the European Photon Imaging Camera (EPIC-pn, Strüder et al. 2001) operated in small window mode to prevent any pile-up. The details of the *XMM-Newton*/EPIC-pn observations of this source are listed in Table 1. We reprocessed the raw data to level 1 data for EPIC-pn by Scientific Analysis System (SAS v16.1.0³) with calibration files dated February 2, 2018. We have used only the unflagged (FLAG == 0) events for excluding the edge of CCD and the edge of the bad pixel. Besides this, we also use PATTERN ≤ 4 for single and double

pixel. We exclude the photon flares by proper GTI files to acquire the maximum signal-to-noise ratio. After that, we use an annular area of 30 arcsec outer radii and 5 arcsec inner radii centered at the source to extract the source event. For the background, we use a circle of 60 arcsec in the lower part of the window that contains no (or negligible) source photons. The response files (*arf* and *rmf* files) for each EPIC-pn spectral data set were produced with SAS tasks ARFGEN and RMFGEN, respectively. The GRPPHA task is used with 100 counts per bin for 0.3–10.0 keV EPIC-pn spectra.

2.2 *Suzaku*

Suzaku observed Ark 120 on 2007 April 1 (Obs ID: 702014010) in HXD normal position with exposure of ~101 ks using X-ray imaging spectrometer (Koyama et al. 2007) and ~89 ks for Hard X-ray Detector (Takahashi et al. 2007). The photons were collected in both 3 × 3 and 5 × 5 editing modes. From this observation, a presence of soft-excess emission in soft X-ray was reported by (Nardini et al. 2011). Also, Fe K α emission line with full-width at half maximum of 4700^{+2700}_{-1500} km s⁻¹ was previously reported by (Nardini et al. 2016) by using *Suzaku* observation along with *XMM-Newton*, *Chandra*, and *NuSTAR*.

³<https://www.cosmos.esa.int/web/xmm-newton/sas-threads>

We use the standard data-reduction technique for *Suzaku* data analysis illustrated in *Suzaku* Data Reduction Guide⁴ and followed the recommended screening criteria while extracting *Suzaku*/XIS spectrum and light curves. The latest calibration files⁵ available (2014-02-03) using FTOOLS 6.25 is used to reprocess the event files. The source spectra and light curves are extracted from a circular region of radius 200 arcsec centred on the Ark 120 and the background region is selected on the same slit with a circular region of 250 arcsec. Finally, we merge the two front illuminated detectors (XIS0 and XIS3) to produce the final spectra and light curves for Ark 120. We generated the response files through XISRESP script. We have ignored the Si K edge in the *Suzaku* detector by neglecting the data in the energy range of 1.6 to 2.0 keV. The GRPPHA task is used with 50 counts per bin for the XIS spectra.

As *Suzaku* has a high energy X-ray detector (HXD), we use the HXD/PIN data for our analysis. We reprocessed the unfiltered event files using the standard tools. The output spectrum and light curves are extracted by using the `hxdpinxbpi` and `hxdpinxblc`, respectively. Further, we correct the spectrum to take into account both the non-X-ray and the cosmic X-ray backgrounds and the dead time correction. The GRPPHA task is used with 1 count per bin for the HXD spectra.

2.3 NuSTAR

NuSTAR (Harrison et al. 2013) observed Ark 120 simultaneously with *XMM-Newton* with FPMA and FPMB on 2013 February 18 (N1) and 2014 March 22 (N2) for the exposure of ~ 166 and ~ 131 ks, respectively. The details of the observation log are given in Table 1. We consider both N1 and N2 observations for our analysis. (Porquet et al. 2018, 2019) used this data along with *XMM-Newton* and determined the spin $0.83^{+0.05}_{-0.03}$ and comment on the dimension of the corona and temperature by analyzing these X-ray data.

The level 1 data is produced from the raw data by using the *NuSTAR* data analysis software (NuSTARDAS v1.8.0). The cleaned event files are produced with standard NUPIPELINE task and calibrated with the latest calibration files available in the *NuSTAR* calibration database (CALDB).⁶ We chose 90-arcsec radii for the source and 180-arcsec radii for the background region on the same detector to avoid contamination and detector edges. For the final background-subtracted light curves, we use 100s bin for both FPMA and FPMB. The response files (*arf* and *rmf* files) are generated by using the `numkrmf` and `numkarf` modules, respectively. The GRPPHA task is used with 10 counts per bin for FPMA/FPMB spectra.

2.4 Swift data

Swift X-ray telescope (XRT; Burrows et al. (2005)), working in the energy range of 0.2 to 10.0 keV, is an X-ray focusing telescope. XRT observed this source in both WT (windowed timing) and pc (photon count) modes depending on the brightness of the source. Ark 120 was observed over ~ 130 times from 2008 July 24 to 2018 January 24. In 2008, *Swift* observed three times, namely, on July 24, July 31 and August 3. We stack the spectra to produce a combined spectrum (XRT1). Then, it again observed on 2014 March 22, which had a simultaneous observation with *XMM* and *NuSTAR*. We consider the XMM3 observation over this particular XRT observation. *Swift*

observed Ark 120 from 2014 September 6 to 2015 March 15 on a nearly daily basis. Further, we stack these observations into four observations (XRT2, XRT3, XRT4, XRT5) with each observations spanning around 50 days. In the last epoch, *Swift* observed Ark 120 from 2017 December 5 to 2018 January 24 over ~ 50 d. We stack the observations to produce the spectra of XRT6. The details of the observation log are stated in Table 1. We use the online tool ‘XRT product builder’⁷ Evans, Beardmore & Page (2009) to extract the spectrum and light curves. This product builder performs all necessary processing and calibration and produces the final spectra and light curves of Ark 120 in WT and PC mode. The GRPPHA task is used with 10 counts per bin for XRT spectra. The overall lightcurves for the energy range 0.5 to 10.0 keV are presented in Fig. 1. Here we have considered the binsize = 100 s for all lightcurves.

3 SPECTRAL ANALYSIS

We use *XMM-Newton*, *Suzaku*, *NuSTAR*, and *Swift* data for the spectral analysis and explore the spectral variation over ~ 15 yr (2003-2018) period using XSPEC v12.10.1f (Arnaud 1996). We explore the broad spectral properties with *nthcomp* model (Zdziarski, Johnson & Magdziarz 1996). Later, we apply TCAF model (Chakrabarti & Titarchuk 1995) to extract the physical flow parameters such as the accretion rates and size of the Compton cloud.

Along with these models, we use a Gaussian component for the Fe fluorescent emission line. While fitting the data, we use two absorption components, namely TBabs (Verner et al. 1996) and zTBabs (Wilms, Allen & McCray 2000). The component, TBabs is used for the Galactic absorption, where hydrogen column density ($N_{\text{H, gal}}$) is fixed at $9.78 \times 10^{20} \text{ cm}^{-2}$ (Kalberla et al. 2005). To calculate the error for each parameter in spectral fitting with 90 per cent confidence level, we use ‘error’ command in XSPEC.

For HXD spectra, the Cash-statistics (Cash 1979) is more suitable. This is due to very low counts in the HXD spectra where we used unbinned data. In such a case, ~ 1 per bin causes a deviation of ~ 15 per cent from χ -statistics. And, both of the statistics are same for ≥ 10 counts per bin. Thus, for all other detectors the χ -statistics could be applied.

We use the following cosmological parameters in this work: $H_0 = 70 \text{ km s}^{-1} \text{ Mpc}^{-1}$, $\Lambda_0 = 0.73$, and $\Omega_{\text{M}} = 0.27$ (Bennett et al. 2003). With the assumed cosmological parameters, the luminosity distance of Ark 120 is 142 Mpc.

3.1 Nthcomp

We have started the spectral fitting with *nthcomp* model, and the model in XSPEC reads as

$$\text{TBabs} * \text{zTBabs} * (\text{nthcomp} + \text{zGaussian})$$

nthcomp is a thermally Comptonized continuum model proposed by Zdziarski et al. (1996) and later extended by Zycki, Done & Smith (1999). We fit all X-ray spectrum above 3.0 keV by this baseline model. The model depends on the seed photon energy (kT_{bb}), which we consider to be of 3 eV for all spectra. Although, Marinucci et al. (2019) considered kT_{bb} to be 15 eV. It is to be noted that, we vary kT_{bb} from 1 to 50 eV, and failed to notice any deviation in the residuals of the fitted spectra. We consider these seed photons to be disc-blackbody type. For that, we have opted for the *inptype* is 1 for all fits. For the spectral fitting, first, we consider the

⁴<http://heasarc.gsfc.nasa.gov/docs/suzaku/analysis/abc/>

⁵<http://www.astro.isas.jaxa.jp/suzaku/caldb/>

⁶<http://heasarc.gsfc.nasa.gov/FTP/caldb/data/nustar/fpm/>

⁷http://swift.ac.uk/user_objects/

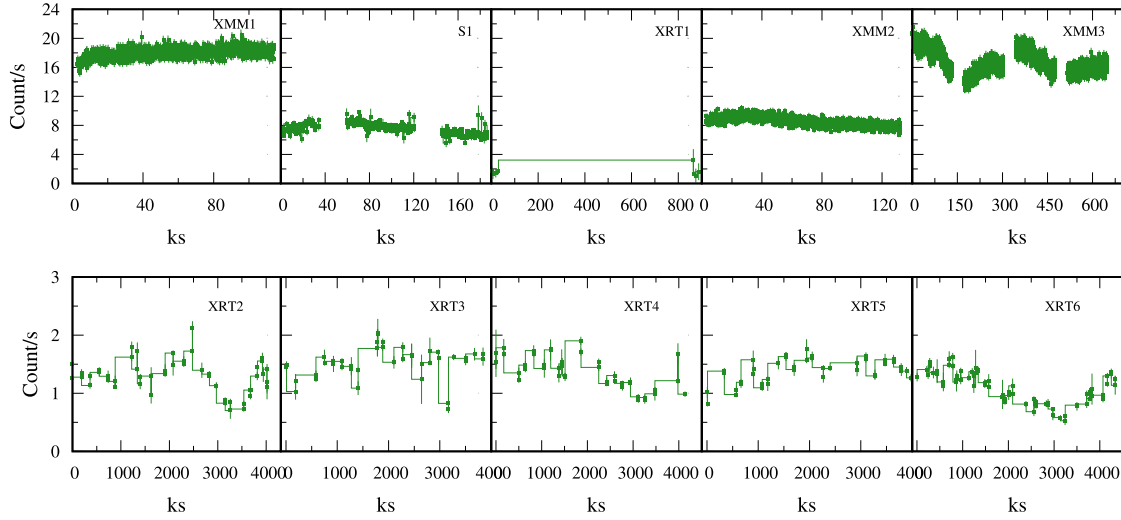


Figure 1. The 15-yr X-ray light-curves having energy range of 0.5–10 keV obtained from various X-ray satellites with time bin of 100s are presented. *XMM-Newton* observed Ark 120 in three epochs. During 2003 and 2013 observations, the exposures were 112.15 and 130.46 ks and the corresponding light curves are marked as XMM1 and XMM2, respectively. In 2014, Ark 120 is observed into four segments by *XMM-Newton*. The combined light curve of 2014 observation is presented as XMM3. *Suzaku* observed this source once in 2007 and it is denoted as S1 in the upper panel. *Swift*/XRT observed 135 times between 2008 to 2018. In 2008, it observed three times (2008 July 24; 2008 July 31 and 2008 August 3) only. To get high-resolution spectra, we added them to make a single observation which is marked as XRT1 and presented in the upper panel. From 2014 September 4 to 2014 October 19, XRT observed Ark 120 20 times. We combined them and marked it as XRT2. We combine 21 and 23 observations observed from 2014 October 22 to December 5 and from 2014 December 9 to 2015 January 1 to make XRT3 and XRT4 observation. From 2015 January 26 to March 15, XRT observed Ark 120 21 times. We denote that as XRT5 observation after combining them. Within 2017 and 2018, Ark 120 was observed by XRT 48 times. We combine them to make the XRT6 observation.

Table 2. *nthcomp* fitting result for the spectrum above 3.0 keV. The optical depth τ is calculated from equation-(1).

ID	MJD	Γ^{nth}	kT_e (keV)	Fe $K\alpha$ (keV)	EW (eV)	χ^2/dof	τ^*
XMM1	52875	$1.90^{+0.01}_{-0.01}$	$159.45^{+81.68}_{-81.69}$	$6.40^{+0.016}_{-0.017}$	116^{+3}_{-4}	312.33/300	0.733 ± 0.003
S1	54191	$2.08^{+0.03}_{-0.03}$	$124.65^{+35.54}_{-35.21}$	$6.38^{+0.052}_{-0.052}$	710^{+10}_{-10}	1117.31/1093	0.726 ± 0.008
XRT1	54676	$1.76^{+0.02}_{-0.08}$	$217.72^{+105.6}_{-112.5}$	—	—	75.68/74	0.671 ± 0.030
XMM2+N1	56341	$1.75^{+0.01}_{-0.02}$	$221.56^{+105.3}_{-107.5}$	$6.42^{+0.061}_{-0.062}$	136^{+8}_{-9}	644.55/641	0.670 ± 0.074
XMM3/a	56734	$1.88^{+0.02}_{-0.02}$	$204.73^{+101.1}_{-105.1}$	$6.47^{+0.056}_{-0.057}$	105^{+10}_{-11}	322.71/336	0.608 ± 0.005
XMM3/b	56736	$1.83^{+0.03}_{-0.02}$	$215.15^{+109.5}_{-110.2}$	$6.31^{+0.012}_{-0.015}$	156^{+10}_{-11}	395.19/319	0.619 ± 0.008
XMM3/c+N2	56738	$1.87^{+0.01}_{-0.01}$	$205.95^{+100.6}_{-99.87}$	$6.37^{+0.052}_{-0.052}$	227^{+12}_{-11}	508.07/469	0.612 ± 0.003
XMM3/d	56740	$1.82^{+0.02}_{-0.02}$	$216.58^{+110.8}_{-112.5}$	$6.46^{+0.064}_{-0.062}$	93^{+05}_{-04}	340.95/332	0.632 ± 0.008
XRT2	56926	$1.60^{+0.01}_{-0.02}$	$274.40^{+136.5}_{-130.8}$	—	—	306.65/290	0.700 ± 0.008
XRT3	56974	$1.84^{+0.02}_{-0.02}$	$215.72^{+105.5}_{-105.8}$	—	—	319.98/320	0.610 ± 0.006
XRT4	57024	$1.72^{+0.02}_{-0.03}$	$225.57^{+109.7}_{-109.9}$	—	—	269.17/280	0.688 ± 0.011
XRT5	57073	$1.88^{+0.02}_{-0.02}$	$201.58^{+99.78}_{-99.20}$	—	—	246.53/261	0.616 ± 0.006
XRT6	58118	$1.65^{+0.02}_{-0.02}$	$246.87^{+120.9}_{-122.8}$	—	—	327.78/318	0.708 ± 0.008

energy range of 3.0 to 10.0 keV. The fitted asymptotic power-law photon index $\Gamma = 1.90$, electron temperature $kT_e = 159.45$ keV and an iron $K\alpha$ line at 6.40 keV with equivalent width (EW) of 116^{+3}_{-4} eV with reduced chi-square (χ^2/dof)=1.04 for degrees of freedom (dof) = 300 is obtained. Next, we analyse the data from the 2007 *Suzaku* observation. We have combined the *Suzaku*/XIS observation with *Suzaku*/HXD and create a spectrum from 0.5 to 40.0 keV. However, we fit 3.0 to 40.0 keV spectrum using the baseline model. The fitted parameters are $\Gamma = 2.08$, $kT_e = 124.65$ keV and iron $K\alpha$ line at 6.38 keV with EW of 710^{+10}_{-10} eV. We have needed an additional powerlaw with powerlaw index 2.46 to take care of high energy (above 10 keV) spectrum. The normalization of the

powerlaw is 0.00093 photons/keV/sec/cm² which is much less compared to the normalization of *nthcomp* in *Suzaku* observation. We have obtained the reduced chi-square (χ^2/dof)=1.02 for degrees of freedom (dof) = 1093 for this fitting. We have fitted the combined spectrum of XMM2+N1 (MJD-56341) and XMM3/c+N2 (MJD-56738) spectrum using this model for the energy range of 3.0 to 79.0 keV with the model parameters such as $\Gamma = 1.75$ and 1.87 and corresponding $kT_e = 221.56$ and 205.95, respectively. We have applied a *zGaussian* for a Fe $K\alpha$ line at $6.42^{+0.061}_{-0.062}$ & $6.37^{+0.052}_{-0.052}$ keV with EWs of 136^{+8}_{-9} & 227^{+12}_{-11} eV for these combined spectra and the (χ^2/dof)=644.55/641 & (χ^2/dof)= 508.07/469, respectively. We have also analysed all other *XMM-Newton* observations in 2014

epoch and found similar result with XMM3/c+N2 observations. For the other three ids (XMM3/a,XMM3/b,XMM3/d), Γ varies within the range of 1.82 to 1.88 with $kT_e = 216.6$ to 204.73. The Fe K_α have also found near ~ 6.4 keV with EW vari from 93 to 227 eV. From more details, see Table-2. Next, we analyse the data obtained from *Swift*/XRT observation for the energy range of 3.0 to 10.0 keV. Fe K_α line is not detected for all the six XRT spectra. We have fitted the *Swift*/XRT spectra by removing the Gaussian component from the baseline model. The power-law index Γ varies from 1.60 to 1.88 and the corresponding electron temperature kT_e varies from 274.40 to 201.58 keV, respectively. The *nthcomp* model fitted spectral analysis result is presented in Table 2. Upon adding all the observations of XRT to create a single spectra, we find the presence of a residual (using power-law model) around 6.2 keV. The EW of the line is 204 eV. And, the line flux (log scale) is $-12.182 \pm 0.05 \text{ erg/cm}^2/\text{s}$. The flux of the iron K_α line is consistent with the observations made by *XMM-Newton* and *Nustar*. However, the flux of the iron K_α line from *Suzaku* is much higher. This could be associated with the highest intrinsic flux of Ark 120 during the 2007 epoch. Furthermore, we calculate the optical depth for each observation using the formula:

$$\tau = \sqrt{\frac{9}{4} + \frac{3}{\theta_e(\Gamma+2)(\Gamma-1)}} - \frac{3}{2}, \quad (1)$$

by inverting the relation A1 is presented in Zdziarski et al. (1996). Here, $\theta_e = \frac{kT_e}{m_e c^2}$ is the electron energy with respect to the rest mass energy. The value of optical depth τ for each observation is provided in Table 2. The maximum error in optical depth is obtained from $\Delta\tau \sim (\frac{1}{2} \frac{\Delta\theta_e}{\theta_e} + \frac{\Delta\Gamma}{\Gamma}) \times \tau$, where $\Delta\theta_e$ and $\Delta\Gamma$ are considered from the fitted errors presented in Table 2.

We address the issue of soft-excess (<3 keV) part by adding another powerlaw component. We freeze the Γ obtained earlier while fitting the primary continuum alone. The second power-law fits the soft-excess, and the results are presented in Table 3. It should be noted that the spectral index of soft-excess (Γ^{SE}) is higher than the spectral index of the primary continuum (Γ^{PC}) for every observation. The long-term variations of spectral index, temperature of the electron cloud, optical depth, and flux within 0.5 to 10 keV range are presented in Fig. 4.

3.2 TCAF

From the *nthcomp* model fitting, we have extracted several valuable pieces of information on the spectral hardness and electron temperature of the emitting system in a time duration of ~ 15 yr. We have also calculated the optical depths from these parameters, which are shown in Table 2. However, the fundamental properties, such as the central black hole mass, accretion rates, the size of the Compton cloud radius could provide a deeper physical understanding of the system. To estimate these quantities, we use the TCAF model (Chakrabarti & Titarchuk 1995) for our spectral analysis. For the spectral fitting, the model in XSPEC reads as

$$\text{TBabs} * \text{zTBabs} * (\text{TCAF} + \text{zGaussian})$$

TCAF is based on one black hole parameter and four flow parameters: (i) black hole mass in units of the solar mass (M_\odot); (ii) Keplerian disc accretion rate (\dot{m}_d) in units of the Eddington rate (\dot{M}_{EDD}); (iii) Sub-Keplerian halo accretion rate (\dot{m}_h) in units of the Eddington rate (\dot{M}_{EDD}); (iv) shock compression ratio (R), and (v) shock location (X_s) in units of the Schwarzschild radius ($r_g = 2GM/c^2$). The upper and the lower limits of all the parameters are put

in a data file called *lmodel.dat* provided in Table 4 as an input to run the source code using *initpackage* and *lmod* task in XSPEC. For the final spectral fitting of a specified observation, we run the source code for less than 10^5 times and select the best spectrum from many spectra using minimization of χ method. First, we start the fitting by the baseline model described as above. Some spectra, such as, the XMM1, S1, XMM2+N1, and XMM3s have high reduced χ^2 ($\chi_{\text{red}}^2 > 2$) value. We noticed that the model has deviated from the actual data at the high energy end. To compensate for that, we have added a powerlaw/pexrav with the baseline model. Thus, the model became

$$\text{T Babs} * \text{zT Babs} * (\text{TCAF} + \text{powerlaw/pexrav} + \text{zGaussian})$$

We have fitted the spectra with this model and found $\chi_{\text{red}}^2 \approx 1$. The variation of χ^2 is shown in Fig. 2 for each model component on the broadband spectrum (0.2-80.0 keV) of Ark 120 during XMM3/c observation. Further, to investigate the source of this power law (whether it is from reflection or not), we have replaced the powerlaw component by pexrav (Magdziarz & Zdziarski 1995). The pexrav model has a power-law continuum with a reflected component from an infinite neutral slab. We have estimated the relative reflection coefficient (R_{ref}) with photon index (Γ_{pexrav}) and cosine of inclination angle $\cos \theta$ from the model fitting. We find θ to vary from 40° to 72° . We fix abundances for heavy elements, such as iron at the Solar value (i.e. 1). For the photon index (Γ_{pexrav}), first, we freeze its value to the value of Γ obtained from *nthcomp*. For this, we have found $\chi_{\text{red}}^2 > 2$. Thereafter, we thaw this parameter and fit it again which have resulted $\chi_{\text{red}}^2 \approx 1$ with new value of Γ_{pexrav} .

We first fit the *XMM-Newton* observation (XMM1) during 2003 (MJD-52875) in the energy range of 0.2 to 10.0 keV with $\text{TBabs} * \text{zTBabs} * (\text{TCAF} + \text{zGaussian})$ model. However, we found a high χ_{red}^2 . The model has deviated from the actual data above 9.2 keV. As already mentioned, we add a powerlaw with the baseline model, and then the powerlaw is replaced by pexrav. The fitted parameters are, $M_{\text{BH}} = 1.5 \times 10^8 M_\odot$, $\dot{m}_d = 0.063$, $\dot{m}_h = 0.112$, $X_s = 20.36$, $R = 1.95$ with $\Gamma_{\text{pexrav}} = 0.14$, $R_{\text{ref}} = 1.96$, and $E_{\text{fold}} = 16.08$ keV and the corresponding $\chi^2 = 1026.20$ with degrees of freedom (dof)= 842. The Fe line is found at 6.4 keV with an EW of 116 eV.

Next, we consider the *Suzaku* observation (S1) of 2007 (MJD-54191). We combine the *Suzaku*/XIS and *Suzaku*/HXD spectra and make a broad-band spectrum in the energy range of 0.5 to 40 keV. We follow the similar steps as described in XMM1 fitting and the fitted parameters are $M_{\text{BH}} = 1.49 \times 10^8 M_\odot$, $\dot{m}_d = 0.126$, $\dot{m}_h = 0.191$, $X_s = 21.44$, $R = 1.66$ with $\Gamma_{\text{pexrav}} = 1.46$, $R_{\text{ref}} = 0.642$, and the corresponding $\chi_{\text{red}}^2/\text{dof} = 1869.89/1673$. The position of Fe line is 6.38 keV with an EW of 710 eV. It is to be noted that, within 6–7 keV range, Nardini et al. (2011) reported the possibility of three lines for XMM1 and two lines for S1 observation, respectively. We find the normalization of TCAF (N_{TCAF} , see Table 5) for *Suzaku* observation (S1) is substantially higher compared to other observations. This could be due to the highest luminosity as exhibited (see Table 3) by the source during 2007 never ever observed by any X-ray satellite.

Following a similar procedure, we fit the broad-band spectra of Ark 120 for the observations during 2013 XMM2+N1 (MJD-56341) and 2014 XMM3/c+N2 (MJD-56738). For these, we have obtained $M_{\text{BH}} = 1.50$ and $1.51 \times 10^8 M_\odot$, $\dot{m}_d = 0.068$ and 0.103 , $\dot{m}_h = 0.111$ and 0.126 , $X_s = 52.83$ and 28.24 , $R = 2.83$ and 2.43 with $\Gamma_{\text{pexrav}} = 0.96$ and 1.66 , respectively. The details of data fitting are given in Table 5. We have separately analysed the four *XMM-Newton* spectra

Table 3. Soft-excess spectral indices are generated while keeping the spectral slope of `nthcomp` (Γ^{nth}) frozen. Intrinsic luminosities are calculated for both of the components using `cplum` in the energy range 0.5 to 10.0 keV.

ID	Γ^{PC} $=\Gamma^{nth}$	$Norm^{PC}$ (10^{-2}) photons/keV/cm ² /s	L^{PC} erg s ⁻¹	Γ^{SE}	$Norm^{SE}$ (10^{-2}) photons/keV/cm ² /s	L^{SE} erg s ⁻¹
XMM1	1.90	$1.16^{+0.04}_{-0.05}$	$44.18^{+0.06}_{-0.07}$	$3.15^{+0.07}_{-0.06}$	$0.58^{+0.02}_{-0.02}$	$43.66^{+0.05}_{-0.04}$
S1	2.08	$18^{+20.3}_{-25.6}$	$45.35^{+0.05}_{-0.05}$	$2.52^{+0.02}_{-0.02}$	$2105^{+10.6}_{-16.5}$	$45.58^{+0.04}_{-0.04}$
XRT1	1.76	$0.66^{+0.03}_{-0.03}$	$43.99^{+0.04}_{-0.04}$	$4.11^{+0.22}_{-0.20}$	$0.84^{+0.10}_{-0.10}$	$43.87^{+0.02}_{-0.03}$
XMM2+N1	1.75	$0.57^{+0.03}_{-0.03}$	$43.93^{+0.05}_{-0.05}$	$3.03^{+0.03}_{-0.02}$	$0.19^{+0.03}_{-0.05}$	$43.16^{+0.03}_{-0.03}$
XMM3/a	1.88	$1.17^{+0.02}_{-0.02}$	$44.19^{+0.02}_{-0.03}$	$3.71^{+0.03}_{-0.03}$	$0.64^{+0.04}_{-0.04}$	$43.71^{+0.02}_{-0.03}$
XMM3/b	1.83	$0.99^{+0.04}_{-0.04}$	$44.14^{+0.03}_{-0.03}$	$3.66^{+0.05}_{-0.05}$	$0.65^{+0.03}_{-0.03}$	$43.61^{+0.05}_{-0.05}$
XMM3/c+N2	1.86	$1.21^{+0.01}_{-0.01}$	$44.90^{+0.04}_{-0.04}$	$4.23^{+0.02}_{-0.02}$	$0.88^{+0.10}_{-0.10}$	$43.19^{+0.04}_{-0.04}$
XMM3/d	1.82	$1.02^{+0.04}_{-0.03}$	$44.16^{+0.04}_{-0.04}$	$4.12^{+0.03}_{-0.03}$	$0.89^{+0.02}_{-0.02}$	$43.88^{+0.06}_{-0.06}$
XRT2	1.60	$0.48^{+0.03}_{-0.03}$	$44.92^{+0.04}_{-0.04}$	$2.92^{+0.19}_{-0.20}$	$0.57^{+0.03}_{-0.04}$	$43.66^{+0.04}_{-0.04}$
XRT3	1.84	$0.79^{+0.03}_{-0.04}$	$44.04^{+0.05}_{-0.05}$	$3.27^{+0.27}_{-0.27}$	$0.47^{+0.06}_{-0.06}$	$43.57^{+0.05}_{-0.05}$
XRT4	1.72	$0.57^{+0.04}_{-0.05}$	$43.94^{+0.04}_{-0.04}$	$2.53^{+0.10}_{-0.12}$	$0.39^{+0.05}_{-0.06}$	$43.54^{+0.04}_{-0.04}$
XRT5	1.88	$0.76^{+0.03}_{-0.03}$	$44.00^{+0.04}_{-0.04}$	$3.17^{+0.34}_{-0.34}$	$0.31^{+0.05}_{-0.05}$	$43.37^{+0.05}_{-0.05}$
XRT6	1.65	$0.42^{+0.02}_{-0.03}$	$43.84^{+0.03}_{-0.03}$	$2.96^{+0.28}_{-0.29}$	$0.23^{+0.02}_{-0.03}$	$43.27^{+0.06}_{-0.05}$

Table 4. The TCAF parameter space is defined in the file `lmod.dat`. The two columns for minima and maxima are provided for the range of iterations. Between them, the first column indicates the soft bound and the second column gives the hard bound of the parameters.

Model parameters	Parameter units	Default value	Min.	Min.	Max.	Max.	Increment
M_{BH}	M_{Sun}	1.0×10^8	2×10^6	2×10^6	5.5×10^9	5.5×10^9	10.0
\dot{m}_d	Edd	0.001	0.0001	0.0001	1.0	2.0	0.0001
\dot{m}_h	Edd	0.01	0.0001	0.0001	2.0	3.0	0.0001
X_s	r_g	100.0	10.0	10.0	1000.0	1000.0	2.0
R		1.5	1.1	1.1	6.8	6.8	0.1

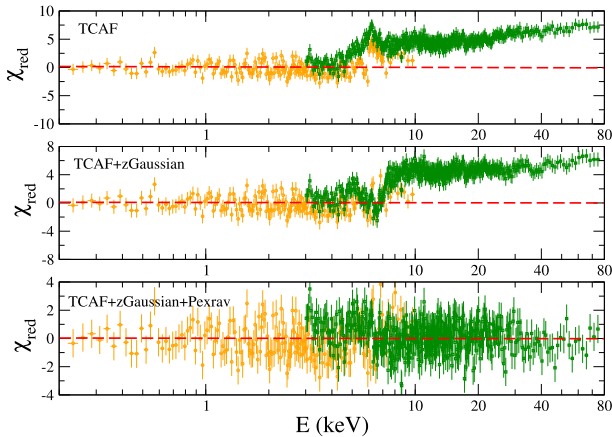


Figure 2. Variation of χ_{red} is shown for each model components on broadband spectra of Ark 120 during XMM3/c observation. Primarily, we have started with TCAF, and then added zGaussian and Pexrav when needed.

during 2014 epoch using TCAF model. We found that the spectral parameters remain similar (see Table 5) for all of the observations.

We fit all the six *Swift*/XRT spectra using the baseline model. Here, we do not find any Fe line in all these spectra. From the fitting, it is noticed that the mass of the central black hole M_{BH} is $1.5 \times 10^8 M_{\odot}$, the disc $\dot{m}_d \sim 0.065$ and halo accretion rates $\dot{m}_h \sim$

0.110 are more or less constant except during the XRT6 observation. Here, we find $\dot{m}_d = 0.081$ and $\dot{m}_h = 0.14$ and the corresponding shock location has moved inward from 57.87 to 42.95 r_g . Therefore, the shock location (X_s) has varied in between 30.0 to 57.87 r_g , and the corresponding variation of the compression ratio (R) is in between 2.6 to 2.8 within September 2014 to January 2018. Here, we do not require any additional powerlaw to fit the high-energy spectra. The details of the parameter variations are presented in Table 5 and Fig. 4. In Fig. 3, we plot the model fitted spectrum with the variation of χ . Detailed discussions on spectral properties are demonstrated in Section 5.1.

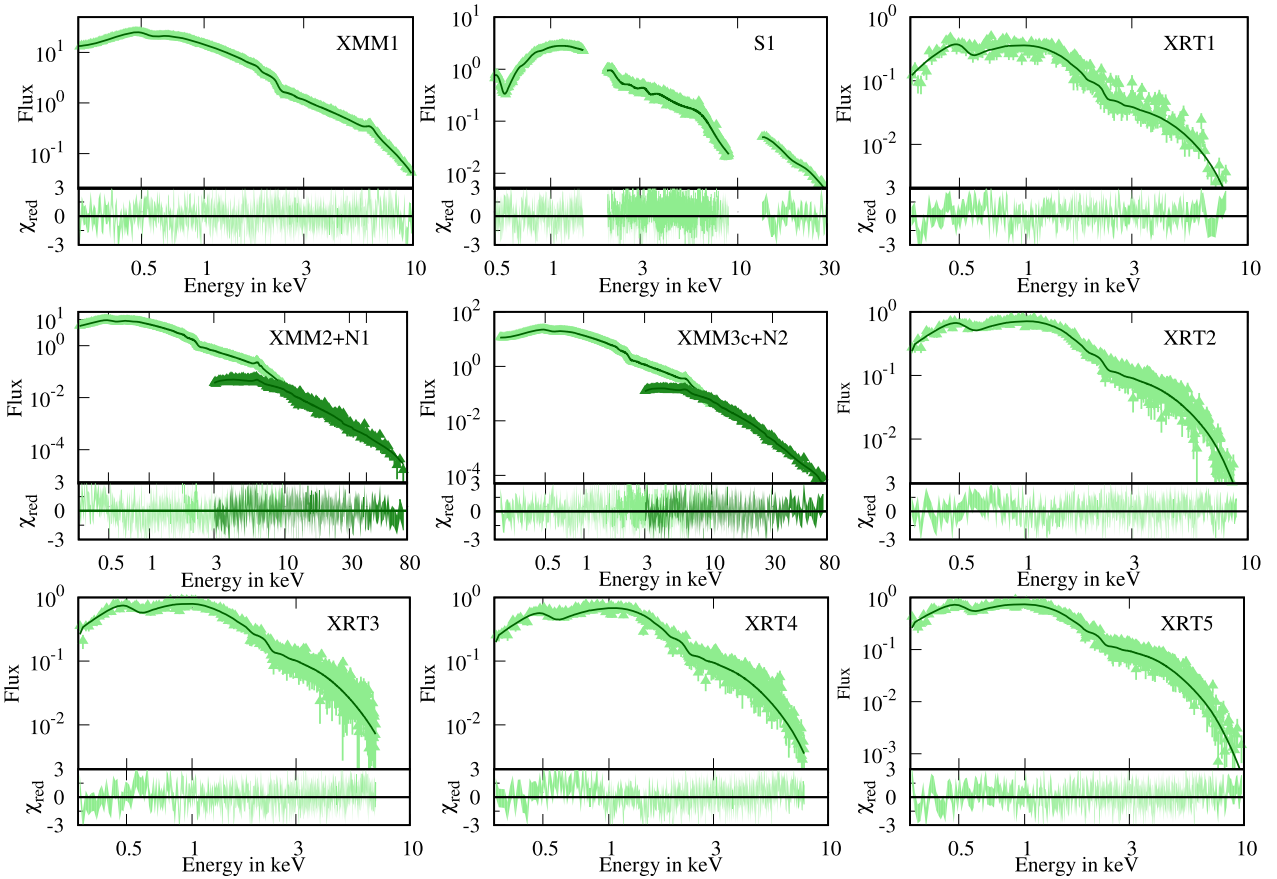
4 TIMING ANALYSIS

4.1 Variability

X-ray variability of an AGN provides a powerful probe of the nearby regions of the central black hole. Since Ark 120 has a ‘bare-type nucleus’, the X-ray comes from the Compton cloud and is not intercepted by any clouds such as BLR, NLR or molecular torus. Thus, the X-ray variability is originated from the varying Compton cloud and the central accretion disc. To analyse the temporal variability in X-ray of Ark 120 in different energy bands, we have estimated different parameters for the duration of 2003 (MJD-52875) to 2018 (MJD-58118). The fractional variability F_{var} (Edelson et al. 1996; Nandra et al. 1997; Edelson et al. 2001; Edelson et al. 2012; Vaughan et al. 2003; Rodríguez-Pascual et al. 1997) of light curves

Table 5. TBabs*zTBabs*(TCAF+pexrav+zGaussian) model fitted Parameters in 0.2–79.0 keV energy band for Ark 120. The TBabs is fixed at $N_{\text{H, gal}} = 9.78 \times 10^{20} \text{ cm}^{-2}$. The third column shows the variation of zTBabs for $z = 0.033$.

ID	MJD	N_{H} (10^{20} cm^{-2})	M_{BH} ($10^8 M_{\odot}$)	\dot{m}_{d} (\dot{m}_{Edd})	\dot{m}_{h} (\dot{m}_{Edd})	X_{s} (r_{g})	R	N_{TCAF} (10^{-3})	Γ_{pexrav}	R_{ref}	N_{pexrav} (10^{-3})	χ^2/dof
XMM1	52875	$1.0^{+0.2}_{-0.2}$	$1.50^{+0.03}_{-0.03}$	$0.063^{+0.002}_{-0.002}$	$0.112^{+0.001}_{-0.001}$	$20.36^{+4.46}_{-4.55}$	$1.95^{+0.34}_{-0.33}$	$0.16^{+0.05}_{-0.05}$	$1.72^{+0.10}_{-0.08}$	$1.96^{+0.05}_{-0.09}$	$0.14^{+0.04}_{-0.05}$	1026.20/842
S1	54191	$1.4^{+0.1}_{-0.2}$	$1.49^{+0.04}_{-0.04}$	$0.126^{+0.002}_{-0.001}$	$0.191^{+0.001}_{-0.001}$	$21.44^{+4.96}_{-4.85}$	$1.66^{+0.54}_{-0.57}$	$233.6^{+54.26}_{-58.65}$	$1.46^{+0.15}_{-0.41}$	$0.642^{+0.71}_{-0.51}$	$5.09^{+1.05}_{-1.03}$	1869.89/1673
XRT1	54675	$1.6^{+0.6}_{-0.4}$	$1.49^{+0.19}_{-0.15}$	$0.064^{+0.005}_{-0.005}$	$0.110^{+0.004}_{-0.003}$	$30.08^{+5.36}_{-6.24}$	$2.80^{+0.54}_{-0.56}$	$0.54^{+0.01}_{-0.02}$	—	—	—	307.78/283
XMM2+N1	54341	$1.9^{+0.3}_{-0.2}$	$1.50^{+0.08}_{-0.07}$	$0.068^{+0.006}_{-0.005}$	$0.111^{+0.004}_{-0.004}$	$52.83^{+8.65}_{-8.56}$	$2.83^{+0.55}_{-0.52}$	$0.57^{+0.02}_{-0.02}$	$0.90^{+0.09}_{-0.10}$	$0.254^{+0.47}_{-0.06}$	$0.25^{+0.06}_{-0.05}$	1230.15/1112
XMM3/a	54734	$2.21^{+0.5}_{-0.4}$	$1.49^{+0.09}_{-0.08}$	$0.101^{+0.007}_{-0.008}$	$0.126^{+0.005}_{-0.006}$	$30.15^{+5.62}_{-5.56}$	$2.44^{+0.65}_{-0.62}$	$0.73^{+0.05}_{-0.04}$	$1.62^{+0.02}_{-0.03}$	$0.90^{+0.05}_{-0.06}$	$0.35^{+0.05}_{-0.05}$	1060.65/882
XMM3/b	54736	$2.19^{+0.3}_{-0.3}$	$1.51^{+0.10}_{-0.09}$	$0.102^{+0.005}_{-0.005}$	$0.127^{+0.005}_{-0.006}$	$29.92^{+7.82}_{-6.95}$	$2.40^{+0.61}_{-0.61}$	$0.72^{+0.04}_{-0.03}$	$1.65^{+0.05}_{-0.08}$	$0.94^{+0.08}_{-0.07}$	$0.13^{+0.04}_{-0.04}$	1092.79/860
XMM3/c+N2	54738	$2.3^{+0.3}_{-0.3}$	$1.51^{+0.09}_{-0.10}$	$0.103^{+0.006}_{-0.005}$	$0.126^{+0.004}_{-0.004}$	$28.24^{+5.04}_{-5.25}$	$2.43^{+0.55}_{-0.58}$	$0.31^{+0.01}_{-0.01}$	$1.66^{+0.19}_{-0.19}$	$0.96^{+0.05}_{-0.56}$	$0.12^{+0.06}_{-0.06}$	1578.92/1359
XMM3/d	54740	$1.99^{+0.4}_{-0.6}$	$1.50^{+0.07}_{-0.07}$	$0.101^{+0.009}_{-0.007}$	$0.120^{+0.008}_{-0.006}$	$30.05^{+6.20}_{-4.82}$	$2.46^{+0.54}_{-0.59}$	$0.45^{+0.07}_{-0.08}$	$1.61^{+0.05}_{-0.04}$	$0.94^{+0.01}_{-0.01}$	$0.11^{+0.02}_{-0.03}$	1088.70/858
XRT2	56926	$2.5^{+0.1}_{-0.1}$	$1.49^{+0.18}_{-0.20}$	$0.068^{+0.005}_{-0.006}$	$0.110^{+0.003}_{-0.003}$	$53.56^{+8.27}_{-8.87}$	$2.73^{+0.51}_{-0.47}$	$0.36^{+0.01}_{-0.02}$	—	—	—	579.89/555
XRT3	56974	$1.9^{+0.5}_{-0.5}$	$1.51^{+0.19}_{-0.20}$	$0.068^{+0.006}_{-0.006}$	$0.110^{+0.004}_{-0.005}$	$55.16^{+8.57}_{-8.80}$	$2.74^{+0.45}_{-0.41}$	$0.25^{+0.01}_{-0.01}$	—	—	—	630.08/594
XRT4	57024	$1.1^{+0.2}_{-0.3}$	$1.50^{+0.15}_{-0.18}$	$0.061^{+0.005}_{-0.006}$	$0.110^{+0.005}_{-0.003}$	$56.86^{+10.97}_{-10.89}$	$2.69^{+0.48}_{-0.47}$	$0.11^{+0.01}_{-0.01}$	—	—	—	702.39/548
XRT5	57073	$1.4^{+0.4}_{-0.3}$	$1.49^{+0.16}_{-0.15}$	$0.069^{+0.006}_{-0.007}$	$0.110^{+0.005}_{-0.005}$	$57.87^{+12.99}_{-12.08}$	$2.77^{+0.52}_{-0.54}$	$0.28^{+0.02}_{-0.01}$	—	—	—	551.49/531
XRT6	58118	$2.0^{+0.4}_{-0.4}$	$1.51^{+0.16}_{-0.15}$	$0.081^{+0.006}_{-0.005}$	$0.140^{+0.006}_{-0.007}$	$42.95^{+8.98}_{-8.20}$	$2.69^{+0.59}_{-0.61}$	$0.22^{+0.01}_{-0.01}$	—	—	—	612.9/589

**Figure 3.** TCAF model fitted spectra of Ark 120 from the *XMM-Newton*, *Suzaku*, *NuSTAR*, and *Swift* observations along with the residuals obtained from the spectral fitting. All spectra are drawn in the rest frame of the AGN.

of x_i count s^{-1} with finite measurement error σ_i of length N with a mean μ and standard deviation σ is given by

$$F_{\text{var}} = \sqrt{\frac{\sigma_{\text{XS}}^2}{\mu^2}},$$

(2)

where σ_{XS}^2 is excess variance (Nandra et al. 1997; Edelson et al. 2002), an estimator of the intrinsic source variance and is given by

$$\sigma_{\text{XS}}^2 = \sigma^2 - \frac{1}{N} \sum_{i=1}^N \sigma_i^2. \quad (3)$$

The normalized excess variance is given by $\sigma_{\text{NXS}}^2 = \sigma_{\text{XS}}^2/\mu^2$. The uncertainties in σ_{NXS}^2 and F_{var} are taken from Vaughan et al. (2003) and Edelson et al. (2012).

The emitted X-ray of Ark 120 in different energy bands (0.5–10.0 keV; 0.2–2.0 keV; 3.0–10.0 keV) have exhibited different degrees of variabilities (Table 6) for a constant time binsize of 100s. From XMM1, the lower energy (0.2–2.0 keV) count rate was initially high ($X_{\text{max}} = 21.95$) in 2003 observation. Then, in 2013 (XMM2), it became half ($X_{\text{max}} = 10.24$) from its initial value. In 2014 (XMM3 combine), the count increased ($X_{\text{max}} = 25.07$). The fractional variability (expressed in per cent) in this energy range increased from 1.6 to 9.8 from 2003 to 2014 observations. A similar trend is shown by σ_{NXS}^2 (0.0003 to 0.0096) in this energy band for each observation of XMM (Table 6). Like low-energy part, the high energy (3.0–10.0 keV) follow the similar type of trend for the count rate and fractional variability. The average value of σ_{NXS}^2 is 0.0019, with a range from 0.0010 to 0.0038. Reeves et al. (2016) observed ionized medium around the nuclear region through the *XMM-Newton*/RGS spectra. They concluded that the medium is most likely to be out of our line of sight. The variability in the low-energy range (0.2–2 keV) could have some contributions from this medium.

We calculate the variability in 0.5–10.0 keV range from the *Suzaku* data. We find higher variability $F_{\text{var}} = 8.6 \pm 0.31$ in the 2007 *Suzaku* data as compared to the previous XMM observations. The variability for XRT observations in 0.5–10.0 keV range are shown in Table 6. Due to the lack of data points, XRT1 observation yields an imaginary value of F_{var} , and is not shown in Table 6. From the other observations of *Swift*/XRT, we observe high fractional variability (F_{var}) from 14.03 to 23.04 with $\langle F_{\text{var}} \rangle = 18.22$. The average value of $x_{\text{max}}/x_{\text{min}}$ and σ_{NXS}^2 for these observations are 2.65 and 0.035 with a range from 2.16 to 3.09 and 0.0197 to 0.0548, respectively. The higher values of F_{var} for *Swift*/XRT observations could be due to the shorter observations span which reduce source amplitude.

4.2 Delay estimation

For temporal analysis of the long-term archival data of Ark 120, we stress three epochs of *XMM-Newton*, 2003, 2013, and 2014 out of which the latter two have high energy (3–80 keV) counterparts observed by *NuSTAR*. We have performed cross-correlation analysis using ICF (Gaskell & Peterson 1987), DCF (Edelson & Krolik 1988), and ζ -discrete cross-correlation function (ZDCF,⁸ Alexander (1997)) for comparison. The likelihood is calculated using 12000 simulation points in the ZDCF code for the light curves obtained by *XMM-Newton*. The peak error is calculated using the formula provided by Gaskell & Peterson (1987). We have followed a similar procedure as in Chatterjee et al. (2020). The time-resolution of each light curve is 1000 s. The 0.2–2 keV light curve obtained from 2003 data yields an acceptable $\chi_{\text{red}}^2 < 1.5$ when fit with a straight line. However, data procured in 2013 and 2014 in a similar energy band have a high residual and are not suitable for linear fitting. All three high energy light curves (3–10 keV) have $\chi_{\text{red}}^2 < 1.5$ when fitted with straight lines. We have carried out the delay estimation using the *XMM-Newton*/Epic-pn data to ensure the simultaneity in their procurements.

The DCF (Edelson & Krolik 1988), performed using the light curves, have generated three distinct patterns. The 2003 data has produced 2.78 ± 16.67 min or ~ 0.16 ks delay. We have fitted the peak

using a Gaussian model (dotted line in Fig. 5). Considering the error, no delay can be seen between two bands of X-ray. Similar delay pattern is also observed from ZDCF, and the likelihood density also maximizes around zero. Likewise, we have performed Gaussian fitting for 2013 data where a positive delay of 78.51 ± 35.17 min or ~ 4.7 ks has been seen between soft and hard X-ray photons using DCF. But, the ZDCF peak maximizes around 112.68 ± 35.22 min or 6.7 ks and likelihood peak coincides with that (see Fig. 5). In 2014 (XMM3/c), the delay sign have switched, and we find a negative delay of -69.19 ± 25.67 min or ~ -4.1 ks between the soft and hard band from DCF analysis. However, ZDCF peaks maximize around two positions, -76.19 ± 25.67 (-4.56 ± 1.54 ks) and -820.19 ± 26.46 (-49.2 ± 1.58 ks) minutes having peak values of 0.664 and 0.722, respectively. Between these two, the former coincides with the DCF pattern (see, Table 7 for details). To resolve the positional uncertainty of the peak, we have added all four light curves of 2014 epoch and performed the DCF and ZDCF on the overall light curve (see Fig. 6). The latter produced significant confidence around the time delay of -2.43 ± 1 from DCF and -2.90 ± 1.26 ks from the ZDCF. The likelihood of the delay pattern for the combined light curve of 2014 suggests a time delay of ~ -1.5 to -4.5 ks. For all three cases, we find the peak values of ZDCF patterns are less than the corresponding peak values obtained from DCF patterns.

5 DISCUSSIONS

We have studied the central region of Ark 120 through X-ray (above 0.2 keV) using the data of *XMM*, *Suzaku*, *NuSTAR*, and *Swift*/XRT in the period 2003 (MJD-52875) to 2018 (MJD-58118). As it is a bare type AGN, the X-ray spectra mainly generated from the nearby region of the central engine.

5.1 Evolution of the source: primary continuum

The ‘bare-type AGN’ Ark 120 was observed for a period of 15 yr, 2003 to 2018 using various X-ray satellites. During these observations, the source has exhibited variability in both spectral and temporal domain. The luminosity of the source in the energy range of 2.0 to 10.0 keV varied within $\sim 10^{43.5} - 10^{45.5}$ erg s⁻¹ throughout these observations. From the *nthcomp* model, we report the variation of the spectral index ($1.6 < \Gamma < 2.08$) where the harder spectra were observed after 2014. Following Vaughan et al. (2004), we have fitted the 2003 spectrum of Ark 120 with (*nthcomp* + Gaussian) model. The fitted $\Gamma = 1.90^{+0.01}_{-0.01}$ agrees with the spectral index previously observed (table 4 of Vaughan et al. 2004) and corresponding temperature of the Compton cloud is $kT_e = 159.45^{+81.68}_{-81.69}$ keV. The (TCF + Gaussian) model provide a few previously unknown parameters like accretion rates, disc rate $\dot{m}_d = 0.063 \pm 0.002$ and halo rate $\dot{m}_h = 0.112 \pm 0.001$. This suggests that the source was initially halo dominated. This behaviour is normal for an AGN. The shock location or the size of the CENBOL (X_s), estimated from the fits, is $20.36 \pm 4.4r_g$. The shock is found to be moderately strong with a compression ratio of $R = 1.95 \pm 0.05$.

The softest spectrum, having $\Gamma = 2.08^{+0.03}_{-0.03}$ is seen during the *Suzaku* observation in 2007. It is to be noted that, Nardini et al. (2011) found the spectral index to be $\Gamma = 2.03^{+0.01}_{-0.04}$ for the *Suzaku* data using blurred reflection model. We have estimated the temperature of the Compton cloud to be $kT_e = 124.65^{+35.54}_{-35.21}$ keV. This is the least of all temperatures obtained from all the observations. Using a single Gaussian, we find the presence of a broad iron line ($6.38^{+0.052}_{-0.052}$) keV having an EW of $EW = 710^{+10}_{-10}$ eV. The derived optical depth is $\tau = 0.726^{+0.008}_{-0.008}$. This suggests an optically thin Compton cloud.

⁸ ZDCF : <http://www.weizmann.ac.il/particle/tal/research-activities/software>

Table 6. Variability statistics in various energy ranges are shown in this table. We have opted for 100s time bins for variability analysis. In some cases, the average error of observational data exceeds the limit of 1σ , resulting negative excess variance. In such cases, we have imaginary F_{var} , which are not shown in the table.

ID	Energy band keV	N	x_{max} count s $^{-1}$	x_{min} count s $^{-1}$	$\frac{x_{\text{max}}}{x_{\text{min}}}$	σ_{NXS}^2 (10^{-2})	F_{var} (%)
XMM1	0.2–2.0	1117	21.95	19.58	1.12	0.03 ± 0.003	1.6 ± 0.14
XMM2	0.2–2.0	1294	10.24	8.40	1.21	0.31 ± 0.015	5.6 ± 0.40
XMM3/c	0.2–2.0	1309	21.37	17.11	1.25	0.41 ± 0.011	6.4 ± 0.41
XMM3 combine	0.2–2.0	5242	25.07	14.65	1.71	0.96 ± 0.008	9.8 ± 0.10
XMM1	3–10.0	1117	1.95	1.53	1.79	0.10 ± 0.023	3.2 ± 0.04
XMM2	3–10.0	1294	1.22	0.94	1.30	0.12 ± 0.04	3.5 ± 0.55
XMM3/c	3–10.0	1309	3.64	2.92	1.24	0.17 ± 0.001	4.1 ± 0.34
XMM3 combine	3–10.0	5242	2.56	0.92	2.79	0.38 ± 0.027	6.2 ± 0.22
N1	10.0–78.0	722	0.71	0.11	6.75	0.56 ± 0.007	7.5 ± 1.6
N2	10.0–78.0	667	1.71	0.24	7.14	0.12 ± 0.024	3.5 ± 3.6
XMM1	0.5–10.0	1117	20.46	15.26	1.34	0.06 ± 0.007	2.4 ± 0.14
S1	0.5–10.0	586	9.80	5.58	1.76	0.74 ± 0.310	8.6 ± 0.31
XRT1	0.5–10.0	8	3.22	1.67	3.01	-22.3 ± 5.6	–
XMM2	0.5–10.0	1294	10.36	6.73	1.54	0.34 ± 0.021	5.9 ± 0.19
XMM3/c	0.5–10.0	1309	20.13	13.67	1.47	0.34 ± 0.012	5.8 ± 0.15
XMM3 combine	0.5–10.0	5242	21.61	12.87	1.68	0.70 ± 0.011	8.4 ± 0.09
XRT2	0.5–10.0	50	2.13	0.70	3.02	4.28 ± 0.443	20.7 ± 2.3
XRT3	0.5–10.0	43	2.79	1.52	2.79	2.34 ± 0.420	15.3 ± 2.1
XRT4	0.5–10.0	43	1.90	0.88	2.16	3.24 ± 0.460	18.0 ± 2.3
XRT5	0.5–10.0	42	1.77	0.81	2.18	1.97 ± 0.253	14.0 ± 1.8
XRT6	0.5–10.0	72	1.63	0.52	3.09	5.48 ± 0.491	23.4 ± 2.2

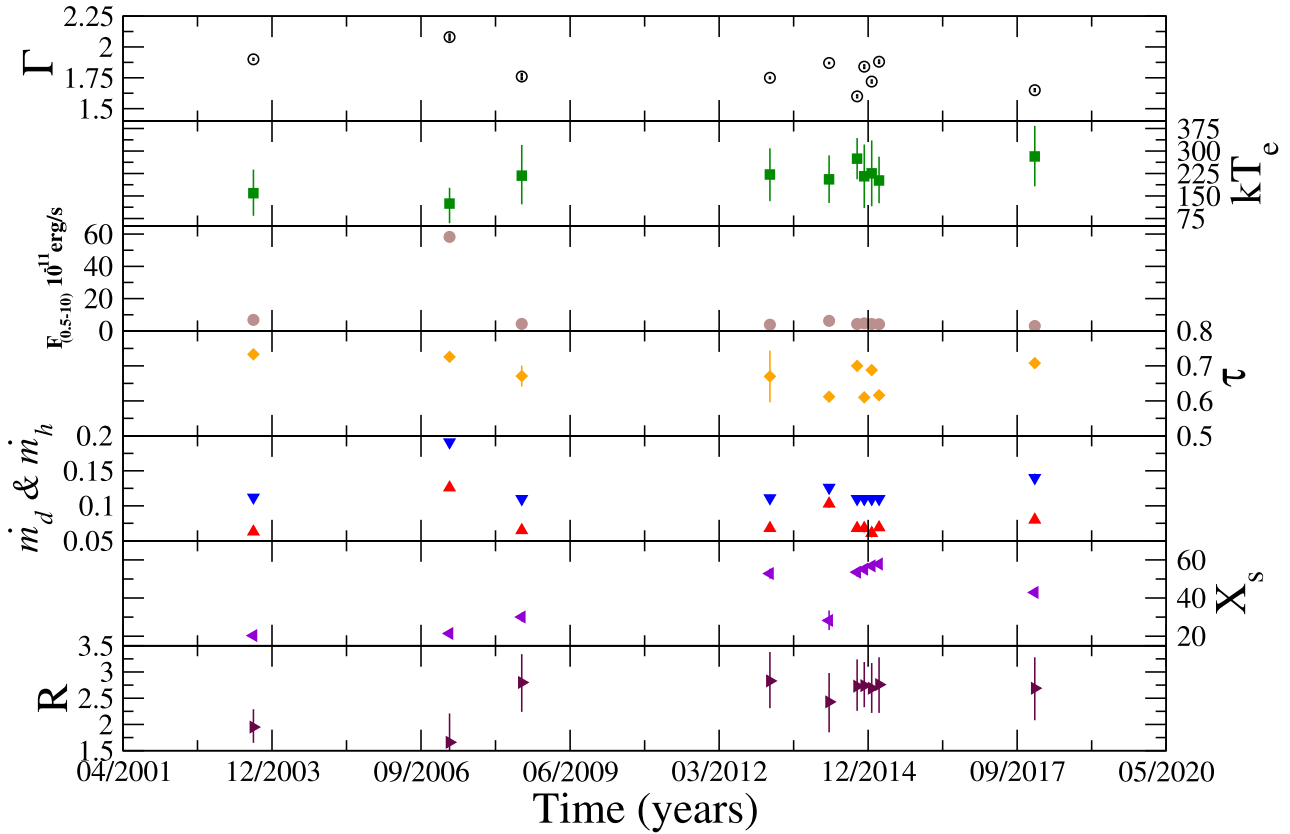


Figure 4. Variation of different model parameters with time are presented.

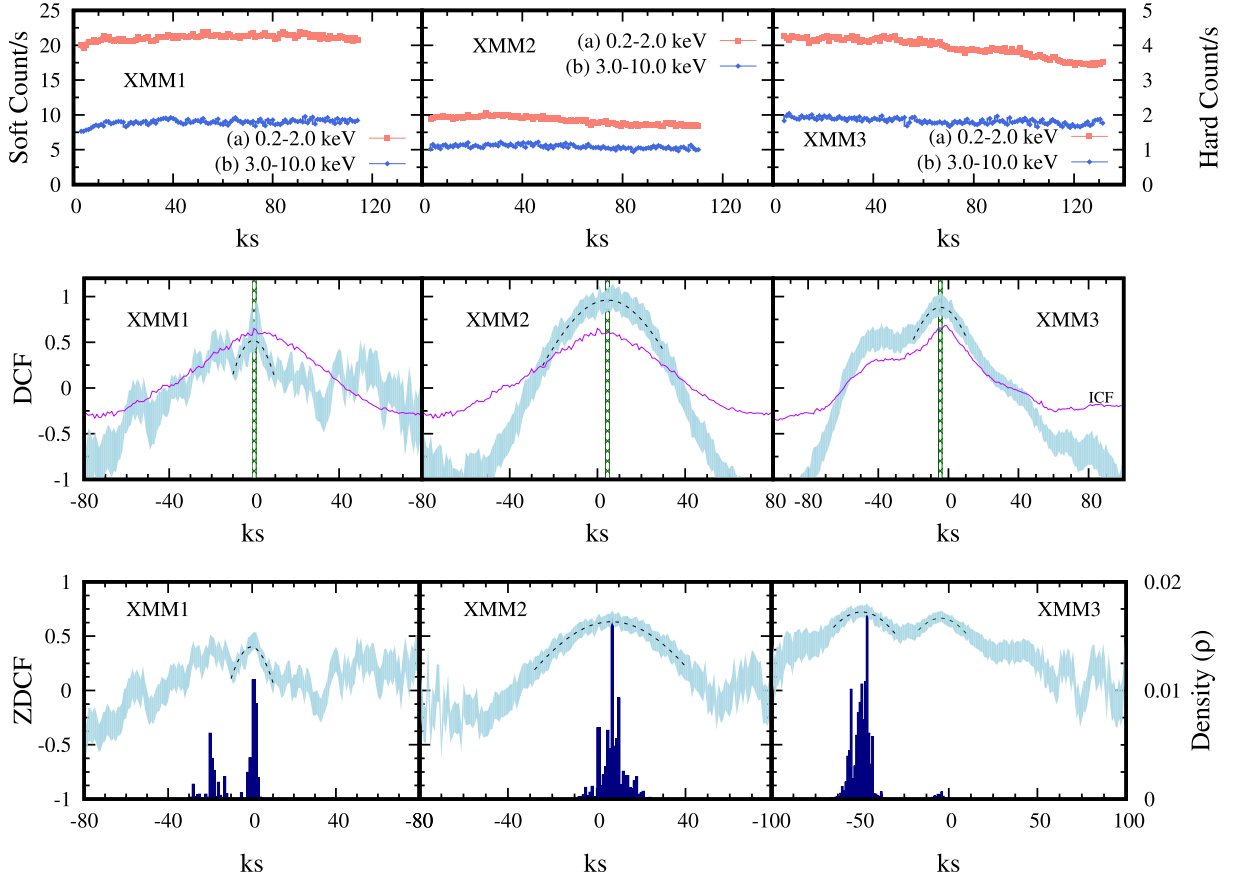


Figure 5. Top panel: The light curves of the energy ranges of 0.2 to 2.0 (light salmon) and 3.0 to 10.0 keV (light blue) observed by *XMM-Newton* are plotted for three epochs. The high energy count always remained a fraction of low-energy counterpart. In 2013, the low-energy count dropped to nearly 50 per cent as compared to 2003. Again in 2014, the 0.2–2 keV count doubled from its value observed in 2013. Middle panel: corresponding discrete cross-correlations between light curves of 0.2–2 and 3–10 keV are plotted. All three epochs exhibited different patterns where *zero*, *positive*, and *negative* delays are observed in 2003, 2013, and 2014, respectively. The ICFs are presented in solid-magenta line. Lower panel: ζ -discrete cross-correlations (light blue) are plotted for light curves of 0.2–2 and 3–10 keV. While 2003 and 2013 patterns remain similar to what have been observed from DCF, the pattern obtained from 2014 data develops twin peak. The likelihoods (dark blue), simulated using 12 000 points, are plotted along with the ZDCF.

Table 7. Parameters used in delay estimations are presented. We used time bin= 1000s (1 ks) for delay estimation between 0.2–2.0 keV versus 3.0–10.0 keV light curves from *XMM-Newton* observations for DCF and ZDCF while time bin=500s (0.5 ks) for ICF. We have considered the larger value between the data binsize and ϵ_τ for the error in measurement of delay. ϵ_τ^d and ϵ_τ^z represents errors for DCF and ZDCF patterns, respectively. ρ_m^i , ρ_m^d , and ρ_m^z represents the maximum values of the cross-correlation functions obtained from ICF, DCF, and ZDCF, respectively. Similarly, τ_{cen}^{icf} , τ_{cen}^{dcf} , and τ_{cen}^{zdcf} represents the centroid values of the cross-correlation functions obtained from ICF, DCF, and ZDCF, respectively. Here, τ_{cen} 's are calculated from the average of all the time delays whose correlation coefficient is greater than $0.8 \times \rho_m$'s.

Id	$\Delta\tau_{d}^{icf}$ (ks)	ρ_m^i	τ_{cen}^{icf} (ks)	ϵ_τ^d (ks)	$\Delta\tau_{d}^{dcf}$ (ks)	ρ_m^d	τ_{cen}^{dcf} (ks)	ϵ_τ^z (ks)	$\Delta\tau_{d}^{zdcf}$ (ks)	ρ_m^z	τ_{cen}^{zdcf} (ks)
XMM1	0.0 ± 1	0.65	1.5	0.388	0.16 ± 1	0.52	-0.35	0.936	-0.057 ± 1	0.45	-0.32
XMM2	0.23 ± 1	0.65	2.23	0.862	4.71 ± 1	0.96	4.6	2.11	6.76 ± 2.11	0.63	6.7
XMM3/c	-1.6 ± 1	0.69	-2.74	0.622	-4.15 ± 1	0.88	-4.60	1.54	-4.56 ± 1.54	0.67	-4.49
XMM3/c	–	–	–	–	–	–	–	1.58	-49.2 ± 1.58	0.72	-49.13
XMM3 combine	–	–	–	0.93	-2.43 ± 1	0.69	2.42	1.26	-2.91 ± 1.26	0.62	-2.90

From the TCAF fits, we find that the size of the Compton cloud has slightly increased to $X_s = 21.44 \pm 4.9r_g$ from the earlier observation. Corresponding disc rate, which enhances the soft seed photons, has increased to $\dot{m}_d = 0.126$. Also, the halo rate has increased to $\dot{m}_h = 0.191$. However, shock strength has decreased (see Table 5). The drop in the kT_e could be understood easily from TCAF, where the increase in disc rate leads to an enhanced cooling fraction. Thus, within the epochs of 2003 and 2007, the temperature of the Compton

cloud varied from 159.45 to 124.65 and as a result, the spectrum get softened.

Later, in 2008, *Swift* observed the source where the spectrum hardened from the previous observation having $\Gamma = 1.76^{+0.02}_{-0.08}$, $kT_e = 217.72^{+105.6}_{-112.5}$ keV, and optical depth $\tau = 0.671^{+0.030}_{-0.030}$. The iron line could not be detected from the XRT spectrum. Corresponding, TCAF fitted parameters, such as the shock location $30.08r_g$ and $R = 2.80$ while \dot{m}_d and \dot{m}_h have changed to 0.064 and 0.11, respectively.

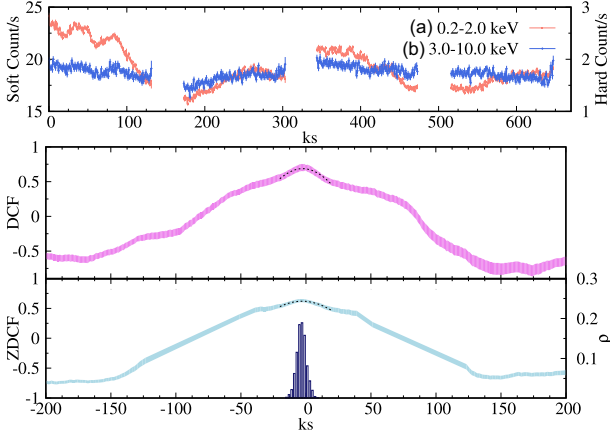


Figure 6. Top panel: The light-curves of the energy ranges of 0.2 to 2.0 keV (light salmon) and 3.0 to 10.0 keV (light blue) observed by *XMM-Newton* are plotted for 2014 epoch. Variability in the soft and hard count rate can be observed profoundly in 2014 (a) where the maximum count rate is 1.5 times of minimum count rate. Middle panel: corresponding discrete cross-correlations between light curves of 0.2–2 and 3–10 keV are plotted. We have also presented the ICF using solid-magenta line. Lower panel: ζ -discrete cross-correlations (light blue) are plotted for light curves of 0.2–2 and 3–10 keV. The likelihoods (dark blue), simulated using 12 000 points, are plotted along with the ZDCF.

Significant variation of spectral properties is also noted during 2013 (XMM2+N1) and 2014 (XMM3/c+N2). The broad-band spectra (3–78) keV are fitted with ($\text{nthcomp} + \text{Gaussian}$) having the spectral indices $1.75^{+0.01}_{-0.02}$ and $1.87^{+0.01}_{-0.01}$ and are in good agreement with parameters obtained by Porquet et al. (2018), Marinucci et al. (2019). The optical depth is reduced from $\tau = 0.670 \pm 0.074$ to 0.612 ± 0.003 . The flux in 2–10 keV band has doubled within a year. The spectral softening could be explained by the drop of temperature of the Compton cloud. However, the decrease in the optical depth for March 2014 data with respect to 2013 has also been seen from Monte Carlo simulations (Marinucci et al. 2019). From TCAF fitting, we find a distinct variation of the flow parameters. The \dot{m}_d changed from 0.068 to 0.103, \dot{m}_h changed from 0.111 to 0.126, and X_s changed from 52.83 to 28.24 within 2013 and 2014 observations, respectively. As the disc accretion rate increases, Compton cooling increases, and this lead to the decrease in the X_s which finally softens the spectrum. Considering TCAF, the lower optical depth for softer spectrum could be explained by the weakening of the shock ($R = 2.43$ as compared to $R = 2.83$ in February 2013) for this observation. The stronger shock creates a distinct boundary between the halo and CENBOL region where the majority of the hard photons are produced. However, for the weaker shock, the CENBOL boundary is less sharp and a fraction of inverse Comptonization could occur within the halo component. Thus, the effective optical depth of the medium could become lower even though the spectrum has softened.

Ark 120 has shown significant variability after February 2014 and is monitored by *Swift*. We have tabulated the spectral and temporal variability in Tables 2 and 5. During September–October of 2014, we find that the spectral slope was $\Gamma = 1.60^{+0.01}_{-0.02}$ and the corresponding temperature was 274.40 ± 130.0 keV, which was maximum within the duration of our observation. From the TCAF fitting, we find \dot{m}_d and \dot{m}_h has changed to 0.068 and 0.11, respectively, and the corresponding shock location has changed to $53.56 \pm 8.2r_g$ and the shock strength has changed from 2.43 ± 0.5 to 2.73 ± 0.5 as observed during February 2014. Later, in December 2014, the spectrum has softened with $\Gamma = 1.84 \pm 0.02$ with the temperature of

Compton cloud 215.72 ± 105.5 keV. The corresponding shock has moved outward and observed at $55.16r_g$ and $R = 2.74$. Like previous observations, we see the halo rate and disc rates are fixed at 0.11 and 0.068, respectively.

XRT4 and XRT5 observations were made starting from the end of December 2014 to March of 2015. During this time, the spectral indices are 1.74 and 1.88, respectively. The temperature and optical depths have also varied during this time. From TCAF fitting, we find the halo rate has decreased to 0.061 in the XRT4 observation. However, the disc rate was constant. Again in XRT5 observation, halo rate has increased to 0.069 while the disc rate remained the same. The shock location and the compression ratio remained constant (considering the errors) within this period. Thus, we can see that Ark 120 exhibited spectral variability (see Fig. 4) within ~ 200 d (since September 2014–March 2015).

In XRT6, which was observed from December 2017 to January 2018, the spectrum of Ark 120 has hardened with respect to the earlier observations during January 2015. The spectral index and temperature of Compton cloud are 1.65 ± 0.02 and 246.87 ± 121 keV, respectively. From TCAF fitting, we find the disc and halo rates have increased to $\dot{m}_d = 0.081$ and 0.14, respectively, and the corresponding shock location settled at $42.95 \pm 8.0r_g$.

In Fig. 7, we have plotted the correlations of a few spectral parameters. We find the spectral index and the temperature of the Compton cloud are anticorrelated (Fig. 7a with Pearson Correlation Co-efficient (PCC) = -0.94) for the long-term observation. This is a well-established relation and are generally found in case of AGNs and Galactic black holes (see Ghosh, Chakrabarti & Laurent 2009; Chatterjee, Chakrabarti & Ghosh 2017a; Jana et al. 2020). However, the values of kT_e are poorly constrained with respect to spectral indices. In Fig. 7(b), we have presented the correlation between shock compression ratio and optical depth. We find $R - \tau$ produces anticorrelation having PCC = -0.49 . In general, stronger shocks are associated with the harder spectra where the optical depth is expected to be less (Chatterjee et al. 2016) and the corresponding shock location is also expected to be bigger. Keeping that argument, we also show the $X_s - \tau$ correlation where an weak anticorrelation (PCC = -0.12) has been observed from the long-term data and presented in Fig. 7(c). The spectrum softens due to the reduction of the shock location X_s , i.e. the size of the Compton cloud (Chakrabarti & Titarchuk 1995; Dutta & Chakrabarti 2010), we find a global trend of anticorrelation (PCC = -0.57) between $X_s - \Gamma$ (see Fig. 7d) for Ark 120.

From the nthcomp fitting, it can be found that the Compton cloud of the source was optically thin for the entire period of observation. Overall, we also noticed that the disc and halo rate is nearly constant and they are ~ 0.07 and ~ 0.11 , respectively, for the majority of observations. But, we find a higher disc and halo rate in 2007 and 2014 observation. The shock location and the compression ratio have varied with time. The variation of these parameters is shown in Fig. 4. First, the shock location, which is also the boundary of Compton cloud in TCAF, increases with time from 20 to $52r_g$ in the first ~ 10 yr. Then the shock location falls to $26.7r_g$ within the next ~ 13 months. Later, we find that the shock location again moves outward from 26.7 to $57.8r_g$ before moving inward again, and finally settling at $42.95r_g$ in January 2018. The Compression ratio (R), which determines the optical depth of the Compton cloud in conjunction with the accretion rates and shock location, also varies as the shock location (X_s). First, the compression ratio increased from 1.95 to 2.83 in ~ 10 yr. Then, the value of R decreased to 1.67 within next 1 yr. After that, it increased to 2.73 within less than six months and finally reached 2.69 at the end of January 2018.

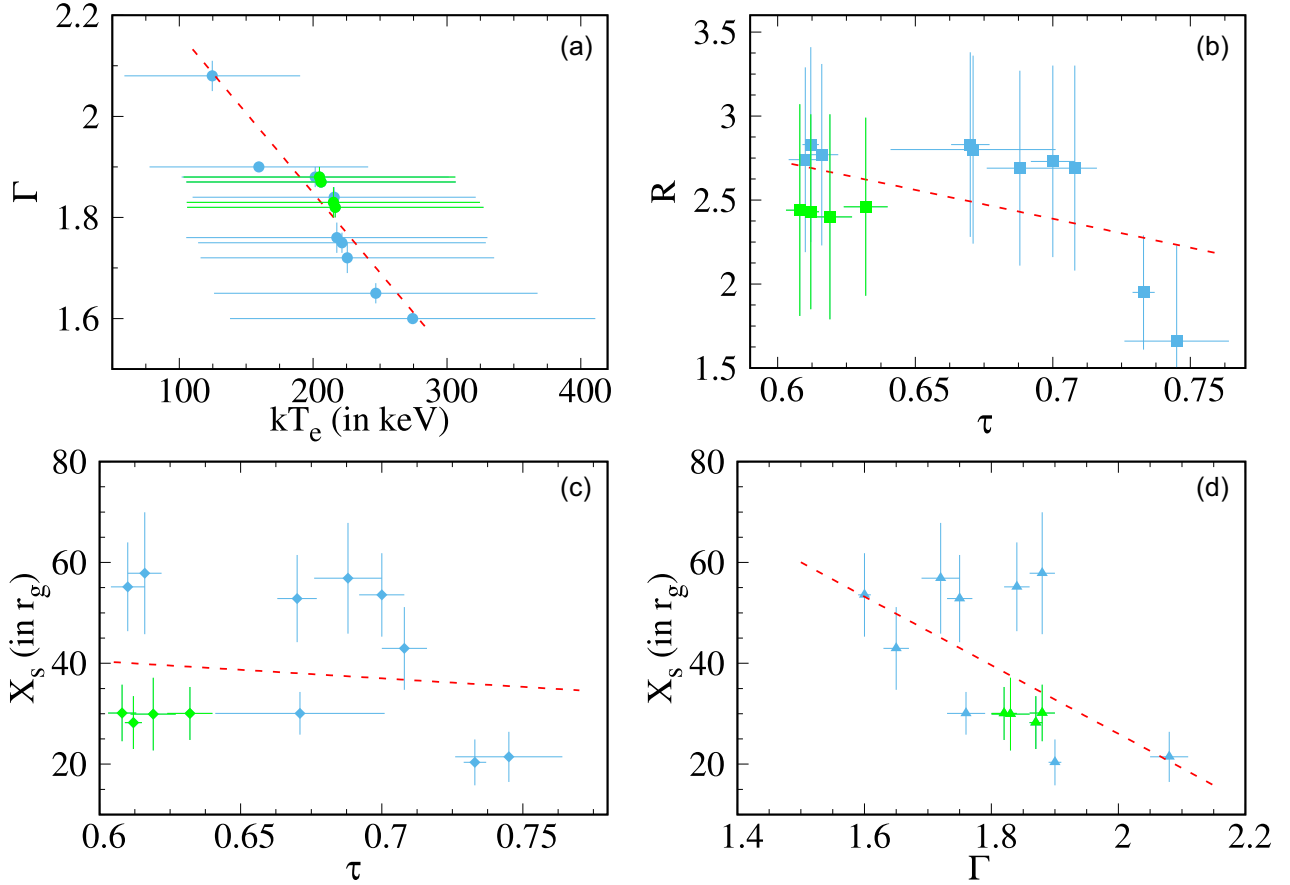


Figure 7. Correlation of fitted parameters are plotted. Panel (a) represents the correlation between Γ versus kT_e and the corresponding PCC is -0.94 . It should also be noted that the errors of kT_e are large. Panel (b) represents the correlation between τ and R . The PCC for these parameters is -0.49 . Panel (c) represents the correlation between τ versus X_s and the corresponding PCC is -0.12 . Panel (d) provides the correlation of Γ versus X_s with PCC -0.57 . The green points represent 2014 observations.

5.2 Evolution of the source: delay patterns

The Compton delay (Payne 1980; Sunyaev & Titarchuk 1980) for an electron cloud of size \mathcal{R} having an optical depth τ and temperature $\theta_e = kT_e/m_e c^2$ can be described by

$$t_c = \frac{\mathcal{R}}{c(1 + \tau)} \frac{\ln(E_h/E_{ss})}{\ln[1 + 4\theta_e(1 + 4\theta_e)]},$$

where c is the velocity of light, E_h and E_{ss} are the energy of hard photons and soft seed photons, respectively. For AGNs having a central black hole mass of $1.5 \times 10^8 M_\odot$ (Peterson et al. 2004), the seed temperature of the photons remains in the 1–10 eV range. The maximum of the hard and soft energy band is considered to be 10 and 1 keV and the seed photon temperature is $E_{ss} = 3$ eV. The light-crossing time for $1r_g$ is $r_g/c = 1.5$ ks for Ark 120. We calculated the delays for the combined parameters obtained from `nthcomp` and `TCAF` model.

We have calculated the Compton delay for XMM1 observation where the size of the Compton cloud is $\sim 20r_g$, optical depth 0.733, and $\theta_e = 0.311$. Substituting the values, we find $t_c^h = 105.3$ ks and $t_c^s = 75.3$ ks which produces a positive theoretical delay of $\Delta\tau = t_c^h - t_c^s = 30$ ks. However, from the observed DCF pattern, we fail to notice any such delay for this case. Here, we find light crossing delay (τ_{lc}) of 30 ks for a $\sim 20r_g$ Compton cloud. The observed zero-delay

could be a combined result of τ_c and τ_{lc} . In that case, it is to be noted that τ_{lc} becomes crucial in presence of a significant contribution of reflection component ($R_{\text{ref}} = 1.96$, see Table 5).

For the broad-band observation (XMM2+N1), the size of the Compton cloud is $\mathcal{R} \sim 50r_g$, having an optical depth of 0.67 and temperature $\theta_e = 0.434$. Combining all these, the maximum hard and soft energy delay which can be generated via Compton scatterings are $t_c^h = 208$ ks and $t_c^s = 148$ ks, respectively. Thus, the maximum delay between hard and soft bands of X-ray can be $\Delta\tau = t_c^h - t_c^s = 60$ ks. The light crossing delay is around $\tau_{lc} = 75$ ks. The combined effects of $\Delta\tau$ and τ_{lc} should yield a negative delay of 15 ks. However, as discussed previously, τ_{lc} could dominate if reflection becomes dominating (here $R_{\text{ref}} = 0.25$). Also, the size of the Compton cloud is much bigger than the what should be the ‘transition radius’ (see, Dutta & Chakrabarti 2016, Dutta, Pal & Chakrabarti 2018 for details) of an AGN having mass $1.5 \times 10^8 M_\odot$. Being an intermediate inclination angle source (Nardini et al. 2011; Marinucci et al. 2019), Comptonization dominates the time delay when the size of the Compton cloud is bigger. The theoretical structure of the Compton cloud is somewhat deviated from the sphere (see, Chakrabarti & Titarchuk 1995) and the thermodynamical fluctuations within the inhomogeneous Compton cloud (see, Chatterjee, Chakrabarti & Ghosh 2017b) contributes to the delay patterns. Considering this, the effect of light crossing delay would be much less and Comptonization

could be considered as the core process, which generates 0.2–2 keV photons during 2013 observations.

In a similar way, we calculate the Compton delay for broadband observation in 2014 (XMM3/c+N2). For that, the size of the Compton cloud $\mathcal{R} = 28 r_g$, the optical depth is $\tau = 0.612$, and $\theta_e = 0.403$. We have obtained $t_c^h = 123.4$ ks and $t_c^s = 88.2$ ks which produces $\Delta\tau = t_c^h - t_c^s = 35$ ks. Contrary to that, the observed delay from XMM3/c is -4.56 ± 1.54 ks. However, combining all the light curves observed by XMM/Newton in 2014 epoch, we find a negative delay of 2.90 ± 1.26 ks. From Fourier lag analysis, Lobban et al. (2018) found a negative delay of 900 s in between the energy domains of 0.3–1 keV and 1–4 keV. The lag estimated by Lobban et al. (2018) was in the frequency domain $4\text{--}10 \times 10^{-5}$ Hz. Since, we have performed the delays independent of frequency and the energy domains are different (e.g. 0.2–2 and 3–10 keV), the resultant magnitude of delay has changed. Nevertheless, it should be noted that negative delays are observed both in time and in the frequency (Fourier) domain. This detection implies the robustness of the lag determination and confirms that the delay in both the domains originated from the same physical mechanism. Clearly, the Comptonization may not be the dominating radiative process for this observation. From Table 5, we see that the reflection co-efficient $R_{\text{ref}} = 0.96$, which refers to a stronger reflection, and could play a major role. Considering the Compton cloud only, τ_{1c} becomes 42 ks, which is comparable to compensate for the positive lag obtained from Comptonization. In this particular case, the maximum possible negative delay would be $\Delta\tau - \tau_{1c} \sim -7$ ks or -116 min. However, the size of the Compton cloud has become bigger and R_{ref} is much less than the XMM1 observation. Thus, the contribution from τ_{1c} could be less effective and we observe a negative delay much less than the maximum allowed delay. It is also to be noted that Lobban et al. (2018) found the X-ray to be leading the U-band by 2.4 ± 1.8 d which they have explained with the light crossing delay.

Thus, along with the spectral variations, we find the delay patterns have varied over the three epochs (2003, 2013, and 2014) in which XMM–Newton observed Ark 120. A significant change in the delay pattern is observed within a year (2013–2014) where the positive delay changed sign and becomes negative with a similar magnitude.

5.3 Soft-excess

The origin of ubiquitous *soft-excess* (Arnaud et al. 1985; Singh et al. 1985; Brandt et al. 1993; Fabian et al. 2002; Gierliński & Done 2004) remains debated. A plausible cause of soft-excess was given using reflection Sobolewska & Done (2007). The multi-wavelength campaign of Mrk 509 (Mehdipour et al. 2011) revealed the correlation of soft-excess with the optical-UV part both in the spectral and temporal domains where they concluded that the soft-excess was generated due to Comptonization by a warm optically thick region surrounding the accretion disc. Done et al. (2012) proposed that the high-mass accretion rate of the disc could generate the soft-excess. For lower L/L_{EDD} , the energy-dependent variability in the soft-excess part was found to be less in case of Narrow line Seyfert 1 galaxies. Lohfink et al. (2012) studied Seyfert 1 galaxy Fairfall 9 where the origin of the soft-excess component was found to be connected with source which generates the broad iron line. However, they implied that another source of Comptonization might be responsible for the formation of the soft-excess.

A strong soft-excess present in the X-ray spectrum of Ark 120 was reported by Brandt et al. (1993), Matt et al. (2014), and Porquet et al. (2004). This soft-excess is also free from the absorbers and was reported by Nardini et al. (2011). As a first step, we investigate

the spectral slopes and the relative contribution of the soft-excess from 2003 to 2018 using the `nthcomp+zGaussian+powerlaw` model and the results are presented in Table 3. Subsequently, we freeze the Γ^{nth} obtained from `nthcomp` while fitting the soft excess below 3 keV. The Γ^{pl} fits the soft-excess < 3 keV. For every observation, we find a soft-excess steeper than the primary continuum (see, Table 3), which is a characteristic associated with the Narrow line Seyfert 1 galaxies. Apart from the steeper power law, the variation of soft-excess luminosity and spectral index can be observed from long-term observations presented in Table 3. We have calculated the intrinsic luminosities of `nthcomp` and `powerlaw` within the energy range of 0.5 to 10.0 keV. In Fig. 8(a), we see a strong correlation ($\text{PCC} = 0.90$) between the intrinsic luminosities of soft-excess ($L_{\text{int}}^{\text{SE}}$) and primary continuum ($L_{\text{int}}^{\text{PC}}$). However, as a ‘bare’ type AGN, Ark 120 has not shown any correlation (Fig. 8b) among the intrinsic luminosities and the line of sight hydrogen column density (N_{H}).

While `nthcomp` provides a good fit in the high-energy range, we have used `TCAF+zGaussian+pexrav` model (presented in Table 5) in the entire range. We find that the TCAF fits well in the range of 0.2–10 and requires no other additional model for the soft-excess part with the range of 0.2–3 keV. The fitted results and residuals are presented in Fig. 3. From the spectral fitting using TCAF, one recognizes that the soft-excess could be originated from the photons which are rarely scattered in the Compton cloud. The surrounding halo will contribute to this energy band (0.2–2 keV). Also, some high energy photons from the Compton cloud which could be reflected from the disc will appear in this energy range after losing their energy through reflection from the cold disc. We have performed Monte Carlo simulations to show the spectral variations with N_s . This is briefly discussed in Section 5.3.1.

5.3.1 Simulated spectra

Radiative and hydrodynamic origin of soft-excess has been investigated in Fukumura et al. (2016) where they proposed that the shock heating near the ISCO could produce the soft-excess. The model reproduced the spectra of ‘bare’ Seyfert 1 galaxy, Ark 120. We have inspected the possibility of scattering dependent spectral contribution from the pre-shock and the post-shock regions (Chakrabarti & Titarchuk 1995). We extend the work of Ghosh et al. (2011), Chatterjee et al. (2018) in case of AGNs considering Ark 120. Using the Total Variation Diminishing (TVD) scheme (Ryu, Chakrabarti & Molteni 1997), we inject matter having a halo rate of 0.1 from the outer boundary at $200r_g$. TCAF fitted parameters are used for the simulation setup and are mentioned in the Fig. 9. Considering the Keplerian disc in the equatorial plane ($z = 0$), we construct the profile of the accretion disc following Shakura & Sunyaev (1973). The Monte Carlo simulation ($0 < r < 100r_g$) has followed the process provided by Pozdnyakov, Sobol & Sunyaev (1983) and later extended by Ghosh et al. (2009) and Chatterjee et al. (2017a). The simulations are performed using 10^7 injected photons for each case. The emergent Comptonized spectra are plotted in Fig. 9. We show the variation of spectral components with respect to the number of scatterings (see also Ghosh et al. 2011) within the region. From Fig. 9, we find that the spectra harden as the number of scatterings increase. The spectrum of the primary component within the energy range of 2.0 to 10.0 keV is dominated by the photons where the number of scatterings is ≥ 10 . However, the soft-excess, the red long-dashed line within 0.2–2 keV, is dominated by the contribution from photons which have suffered ≤ 10 scatterings. A steeper spectral slope (Γ^{SE}) for soft-excess is

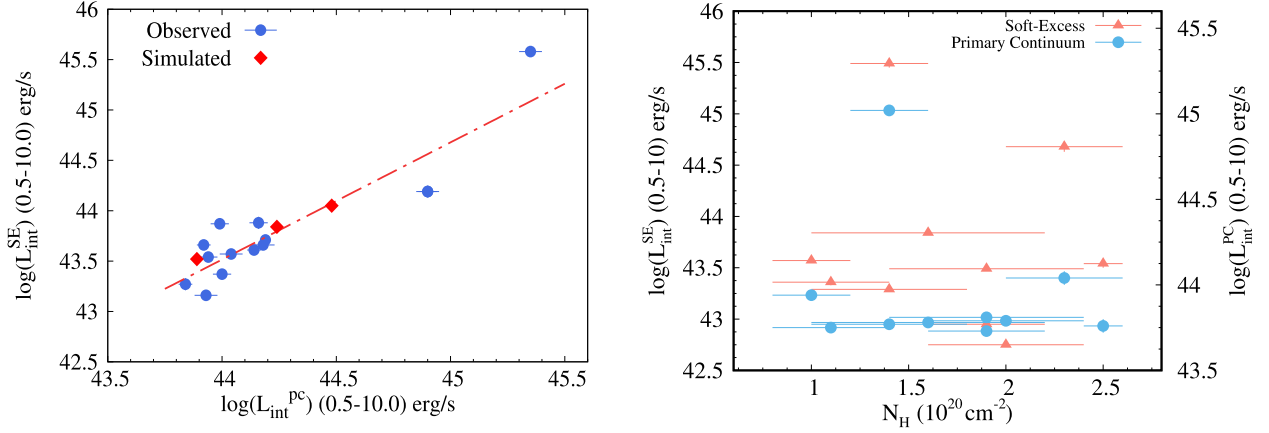


Figure 8. Correlation of intrinsic luminosities of 0.5–10.0 keV obtained using *nthcomp*. Left-hand panel: shows a correlation ($\text{PCC}=0.90$, $p\text{-value} < 0.001$) between the observed intrinsic luminosities of primary continuum and soft-excess (blue circle). Monte Carlo simulated luminosities for both energy ranges are presented with red-diamond points. Right-hand panel: no correlations have been observed between intrinsic luminosities and N_{H} from long-term observations.

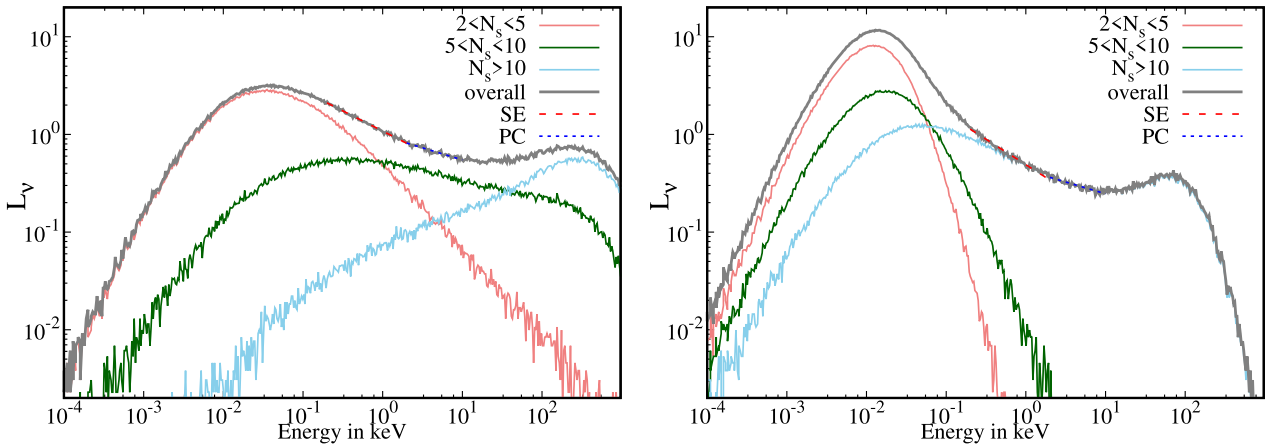


Figure 9. Monte Carlo simulated spectra for Ark 120 are presented. We have considered $M_{\text{BH}} = 1.5 \times 10^8 M_{\odot}$ for Ark 120. Simulation boundary extends up to $100r_{\text{g}}$. For left-hand panel, $m_{\text{d}} = 0.06$; $m_{\text{h}} = 0.1$, $X_{\text{s}} = 60r_{\text{g}}$, and maximum $kT_{\text{e}} = 270$ keV. For right-hand panel $m_{\text{d}} = 0.1$; $m_{\text{h}} = 0.1$, $X_{\text{s}} = 40r_{\text{g}}$, and maximum $kT_{\text{e}} = 100$ keV. Notice the spectral contributions due to increasing number of scatterings. L_{ν} has been normalized with respect to the observed spectrum.

achieved with respect to the primary component (Γ^{PC}) for both of the spectra. This is similar to what has been observed for Ark 120 (Table 3). It is to be noted that, Boissay, Ricci & Paltani (2016) studied 102 Sy1 AGNs and found that there is no link between the reflection and the soft excess. Instead, they indicated that the soft-excess could be related to the thermodynamical properties of Compton cloud and associated medium.

6 CONCLUSIONS

We have studied ~ 15 yr of X-ray data of Ark 120. We find the source varied considerably within that time-span. This source was previously reported to be a ‘bare-type AGN’ and we also find a similar nature of this source from the long-term analysis. The X-ray count rate has increased by a factor of 2 in a few years, and it is not found to be related to the Hydrogen column density (N_{H}) since it is a ‘bare-type AGN’. Following are the major findings from our work.

1. The spectral slopes of the primary continuum (Γ^{PC}) and the soft-excess (Γ^{SE}) are not constant throughout our observational time

span. Γ^{PC} has varied between 1.60 and 2.08 whereas Γ^{SE} between 2.52 and 4.23 from 2003 to 2018.

2. The variation is reflected in fitted parameters of TCAF, namely, the accretion rates and properties of the Compton cloud. From the spectral fitting using TCAF, we find that the disc rate (\dot{m}_{d}) and the halo rate (\dot{m}_{h}) have varied between 0.061 and 0.126 and between 0.108 and 0.191, respectively. The shock location (X_{s}) or the size of the Compton cloud and compression ratio (R) vary correspondingly. X_{s} varies between 20.36 and 57.87, whereas R varies between 1.66 and 2.73.

3. We focused on the simultaneous observations in low (0.2–2.0 keV) and high (3.0–10.0 keV) energy X-ray band from *XMM-Newton* to calculate the time delay between them. We find that in XMM1 observation, there is no delay between the low and high energy band, while a positive delay of 4.71 ± 1 ks is detected in XMM2 observation and a negative delay of 2.9 ± 1.26 ks has been observed from XMM3 observations. A correlated variability among the optical, UV, and X-ray bands has been presented by Lobban et al. (2018; 2020) where negative lag of 900 s within the X-ray and a delay of 2.4 d in between X-ray and UV are reported for 2014 observations which concurs with our findings. Also, Dutta &

Chakrabarti (2016), Chatterjee et al. (2017b) reported in the context of Galactic black holes that the X-ray lag has a strong dependency on the geometric structure of the Comptonization region and orientation of the Keplerian disc (see a review Dutta 2010 for detail) and the net delay is a resultant effect of different physical mechanisms, e.g. Comptonization, reflection, focusing, and jet/outflow emission (Chatterjee et al. 2019; Patra et al. 2019). For the lower inclination and radio-quiet nature of Ark 120, the positive delay could be attributed to the Compton delay while reflection and light-crossing delay could contribute to the negative delay.

4. From the analysis of the long-term data, we report that the luminosity is independent of Hydrogen column density (N_{H}). This is expected as the source has a negligible line-of-sight hydrogen column density ($N_{\text{H}} < 5 \times 10^{20}$). The luminosity of the primary continuum is highly correlated ($\text{PCC} = 0.90$) with the soft excess emission. From TCAF fitting and Monte Carlo simulations using TCAF flow configurations, we show that the soft-excess spectral slope (Γ^{SE}) is the result of a fewer Compton scatterings in the Compton cloud and the primary continuum (Γ^{PC}) is the result of the higher number of Compton scatterings. Corresponding intrinsic luminosities obtained from simulations corroborate with the observed pattern.

ACKNOWLEDGEMENTS

We thank the anonymous referee for insightful comments and constructive suggestions. PN acknowledges CSIR fellowship for this work. AC acknowledges Post-doctoral fellowship of S. N. Bose National Centre for Basic Sciences, Kolkata India, funded by Department of Science and Technology (DST), India. AC has been supported by the Basic Science Research Program through the National Research Foundation of Korea (NRF) funded by the Ministry of Education (2016R1A5A1013277). BGD acknowledges 'TARE' scheme (Ref. No. TAR/2020/000141) under SERB, DST, Govt. of India and also acknowledges Inter-University Centre for Astronomy and Astrophysics (IUCAA) for the Visiting Associate-ship Programme. This research has made use of data and/or software provided by the High Energy Astrophysics Science Archive Research Center (HEASARC), which is a service of the Astrophysics Science Division at NASA/GSFC and the High Energy Astrophysics Division of the Smithsonian Astrophysical Observatory. This work has made use of data obtained from the *Suzaku*, a collaborative mission between the space agencies of Japan (JAXA) and the USA (NASA). This work made use of data supplied by the UK Swift Science Data Centre at the University of Leicester. This work has made use of data obtained from the *NuSTAR* mission, a project led by Caltech, funded by NASA and managed by NASA/JPL, and has utilized the NuSTARDAS software package, jointly developed by the ASDC, Italy and Caltech, USA. This research has made use of the NASA/IPAC Extragalactic Database (NED) which is operated by the Jet Propulsion Laboratory, California Institute of Technology, under contract with the National Aeronautics and Space Administration. This research has made use of the SIMBAD database, operated at CDS, Strasbourg, France.

DATA AVAILABILITY

We have used archival data for our analysis in this manuscript. All the software used in this manuscript are publicly available. Appropriate links are given in the manuscript.

REFERENCES

- Alexander T., 1997, *Astron. Time Ser.*, 218, 163
 Alloin D., Boisson C., Pelat D., 1988, *A&A*, 200, 17
 Arnaud K. A., 1996, in Jacoby G., Barnes J., eds, ASP Conf. Ser. Vol. 101, *Astronomical Data Analysis Software and Systems V*, Astron. Soc. Pac., San Francisco, 17
 Arnaud K. A. et al., 1985, *MNRAS*, 217, 105
 Bennett C. L. et al., 2003, *ApJS*, 148, 1
 Bianchi S., Guainazzi M., Matt G., Fonseca Bonilla N., Ponti G., 2009, *A&A*, 495, 421
 Boissay R., Ricci C., Paltani S., 2016, *A&A*, 588, A70
 Brandt W. N., Fabian A. C., Nandra K., Tsuruta S., 1993, *MNRAS*, 265, 996
 Burrows D. N. et al., 2005, *Space Sci. Rev.*, 120, 165
 Cash W., 1979, *ApJ*, 228, 939
 Chakrabarti S. K., 1989, *MNRAS*, 240, 7
 Chakrabarti S. K., 1990, *MNRAS*, 243, 610
 Chakrabarti S. K., 1995, in Bohringer H., Morfil G. E., Trumper J., eds, 17th Texas Symp. Relativistic Astrophysics and Cosmology, Accretion Disks in Active Galaxies: The Sub-Keplerian Paradigm, Vol. 759, New York Academy of Sciences, New York, NY, p. 546
 Chakrabarti S. K., Titachuk L. G., 1995, *ApJ*, 455, 623
 Chatterjee D. et al., 2016, *ApJ*, 827, 88
 Chatterjee A., Chakrabarti S. K., Ghosh H., 2017a, *MNRAS*, 465, 3902
 Chatterjee A., Chakrabarti S. K., Ghosh H., 2017b, *MNRAS*, 472, 1842
 Chatterjee A., Chakrabarti S. K., Ghosh H., Garain S., 2018, *MNRAS*, 478, 3356
 Chatterjee A., Dutta B. G., Patra P., Chakrabarti S. K., Nandi P., 2019, *Proceedings*, 17, 8
 Chatterjee A., Dutta B. G., Nandi P., Chakrabarti S. K., 2020, *MNRAS*, 497, 4222
 Condon J. J., Yin Q. F., Thuan T. X., Boller T., 1998, *AJ*, 116, 2682
 Crenshaw D. M. et al., 1999, *ApJ*, 516, 750
 Crummy J., Fabian A. C., Gallo L., Ross R. R., 2006, *MNRAS*, 365, 1067
 Debnath D., Chakrabarti S. K., Mondal S., 2014, *MNRAS*, 440, L121
 Denisshuk E. K., Valiullin R. R., Gaisina V. N., 2015, *Astron. Rep.*, 59, 123
 Dewangan G. C., Griffiths R. E., Dasgupta S., Rao A. R., 2007, *ApJ*, 671, 1284
 Done C., Davis S. W., Jin C., Blaes O., Ward M., 2012, *MNRAS*, 420, 1848
 Doroshenko V. T., Sergeev S. G., Pronik V. I., 2008, *Astron. Rep.*, 52, 442
 Dutta B. G., 2018, *Astrophys. & Space Sci. Proc.*, 53, 257D
 Dutta B. G., Chakrabarti S. K., 2010, *MNRAS*, 404, 2136D
 Dutta B. G., Chakrabarti S. K., 2016, *ApJ*, 828, 101
 Dutta B. G., Pal P. S., Chakrabarti S. K., 2018, *MNRAS*, 479, 2183
 Edelson R. A. et al., 1996, *ApJ*, 470, 364
 Edelson R. A., Krolik J. H., 1988, *ApJ*, 333, 646
 Edelson R., Malkan M., 2012, *ApJ*, 751, 52
 Edelson R., Griffiths G., Markowitz A., Sembay S., Turner M. J. L., Warwick R., 2001, *ApJ*, 554, 274
 Edelson R., Turner T. J., Pounds K., Vaughan S., Markowitz A., Marshall H., Dobbie P., Warwick R., 2002, *ApJ*, 568, 610
 Evans P. A., Beardmore A. P., Page K. L., 2009, *MNRAS*, 397, 1177
 Fabian A. C., Ballantyne D. R., Merloni A., Vaughan S., Iwasawa K., Boller Th., 2002, *MNRAS*, 331, L35
 Fender R. et al., 1999, *ApJ*, 519, L165
 Fender R. P., Belloni T. M., Gallo E., 2004, *MNRAS*, 355, 1105
 Fukumura K. et al., 2016, *ApJ*, 827, 31
 García J. et al., 2014, *ApJ*, 782, 76
 Gaskell C. M., Peterson B. M., 1987, *ApJS*, 65, 1
 Ghosh H., Chakrabarti S. K., Laurent P., 2009, *Int. J. Mod. Phys. D*, 18, 1693
 Ghosh H., Garain S. K., Giri K., Chakrabarti S. K., 2011, *MNRAS*, 416, 959
 Gierliński M., Done C., 2004, *MNRAS*, 349, L7
 Gliozzi M., Papadakis I. E., Grupe D., Brinkmann W. P., R  th C., 2017, *MNRAS*, 464, 3955
 Haardt F., Maraschi L., 1991, *ApJ*, 380, 51
 Haardt F., Maraschi L., 1993, *ApJ*, 413, 507
 Halpern J. P., 1984, *ApJ*, 281, 90
 Harrison F. A. et al., 2013, *ApJ*, 770, 103

- Ho L. C., 2002, *ApJ*, 564, 120
- Ichimaru S., 1977, *ApJ*, 214, 840
- Jana A., Chatterjee A., Kumari N. Nandi P., Naik S., Patra D., 2020, *MNRAS*, 499, 5396
- Jansen F. et al., 2001, *A&A*, 365, L1
- Kalberla P. M. W., Burton W. B., Hartmann D., Arnal E. M., Bajaja E., Morras R., Piöppel W. G. L., 2005, *A&A*, 440, 775
- Kollatschny W., Fricke K. J., Schleicher H., Yorke H. W., 1981a, *A&A*, 102, L23
- Kollatschny W., Schleicher H., Fricke K. J., Yorke H. W., 1981b, *A&A*, 104, 198
- Koyama K. et al., 2007, *Publ. Astron. Soc. Japan*, 59, 23
- Kuehn C. A., Baldwin J. A., Peterson B. M., Korista K. T., 2008, *ApJ*, 673, 69
- Laha S., Dewangan G. C., Kembhavi A. K., 2011, *ApJ*, 734, 75
- Laha S. et al., 2014, *MNRAS*, 441, 2613
- Laha S. et al., 2016, *MNRAS*, 457, 3896
- Laha S. et al., 2021, *Nature Astron.*, 5, 13
- Lobban A. P. et al., 2018, *MNRAS*, 474, 3237
- Lobban A. P. et al., 2020, *MNRAS*, 494, 1165
- Lohfink A. M., Reynolds C. S., Miller J. M., Brenneman L. W., Mushotzky R. F., Nowak M. A., Fabian A. C., 2012, *ApJ*, 758, 67
- Madsen K. K. et al., 2015, *ApJS*, 220, 8
- Magdziarz P., Zdziarski A. A., 1995, *MNRAS*, 273, 837
- Magdziarz P., Blaes O. M., Zdziarski A. A., Johnson W. N., Smith D. A., 1998, *MNRAS*, 301, 179
- Mandal S., Chakrabarti S. K., 2008, *ApJ*, 689, L17
- Marinucci A. et al., 2019, *A&A*, 623, A12
- Markoff S., Nowak M. A., Wilms J., 2005, *ApJ*, 635, 1203
- Marziani P., Calvani M., Sulentic J. W., 1992, *ApJ*, 393, 658
- Matt G. et al., 2014, *MNRAS*, 439, 3016
- Mehdipour M. et al., 2011, *A&A*, 534, A39
- Nandi P., Chakrabarti S. K., Mondal S., 2019, *ApJ*, 877, 65
- Nandra K., George I. M., Mushotzky R. F., Turner T. J., Yaqoob T., 1997, *ApJ*, 476, 70
- Nardini E., Fabian A. C., Reis R. C., Walton D. J., 2011, *MNRAS*, 410, 1251
- Nardini E. et al., 2016, *ApJ*, 832, 45
- Patra D., Chatterjee A., Dutta B. G., Chakrabarti S. K., Nandi P., 2019, *ApJ*, 886, 137
- Payne D. G., 1980, *ApJ*, 237, 951
- Peterson B. M. et al., 2004, *ApJ*, 613, 682
- Peterson B. M. et al., 1998, *ApJ*, 501, 82
- Popović L. C., Stanić N., Kubišela A., Bon E., 2001, *A&A*, 367, 780
- Porquet D., Reeves J. N., O'Brien P., Brinkmann W., 2004, *A&A*, 422, 85
- Porquet D. et al., 2018, *A&A*, 609, A42
- Porquet D. et al., 2019, *A&A*, 623, A11
- Poutanen J., Svensson R., 1996, *ApJ*, 470, 249
- Pozdnyakov A., Sobol I. M., Sunyaev R. A., 1983, *Astrophys. Space Sci. Rev.*, 2, 189
- Pringle J. E., Rees M. J., Pacholczyk A. G., 1973, *A&A*, 29, 179
- Reeves J. N. et al., 2016, *ApJ*, 828, 98
- Rodríguez-Pascual P. M. et al., 1997, *ApJS*, 110, 9
- Ross R. R., Fabian A. C., 2005, *MNRAS*, 358, 211
- Ryu D., Chakrabarti S. K., Molteni D., 1997, *ApJ*, 378, 388
- Schulz H., Rafanelli P., 1981, *A&A*, 103, 216
- Shakura N. I., Sunyaev R. A., 1973, *A&A*, 24, 337
- Singh K. P., Garmire G. P., Nousek J., 1985, *ApJ*, 297, 633
- Sobolewska M. A., Papadakis I. E., 2009, *MNRAS*, 399, 1597
- Sobolewska M. A., Done C., 2007, *MNRAS*, 374, 150
- Stanić N., Popović L. C., Kubišela A., Bon E., 2000, *Serb. Astron. J.*, 162, 7
- Strüder L. et al., 2001, *A&A*, 365, L18
- Sunyaev R. A., Titarchuk L. G., 1980, *A&A*, 86, 121
- Takahashi T. et al., 2007, *Publ. Astron. Soc. Japan*, 59, 35
- Titarchuk L., 1994, *ApJ*, 434, 570
- Vasudevan R. V., Fabian A. C., 2007, *MNRAS*, 381, 1235
- Vasudevan R. V., Mushotzky R. F., Winter L. M., Fabian A. C., 2009, *MNRAS*, 399, 1553
- Vaughan S. et al., 2003, *MNRAS*, 345, 1271
- Vaughan S. et al., 2004, *MNRAS*, 351, 193
- Verner D. A., Ferland G. J., Korista K. T., Yakovlev D. G., 1996, *ApJ*, 465, 487.
- Ward M. et al., 1987, *ApJ*, 315, 74
- Weisskopf M. C., et al., 2016a, *Proc. SPIE*, 9905, 990517
- Wilms J., Allen A., McCray R., 2000, *ApJ*, 542, 914
- Zdziarski A. A., Johnson W. N., Magdziarz P., 1996, *MNRAS*, 283, 193
- Zycki P. T., Done C., Smith D. A., 1999, *MNRAS*, 309, 561

This paper has been typeset from a \LaTeX file prepared by the author.